UNDERSTANDING URBAN HEAT ISLAND BY ASSESSING LAND SURFACE TEMPERATURE AND SURFACE PARAMETERS ACROSS DIFFERENT BUILT-UP CLASSES

BADAL KUMAR DASH
JUNE, 2015

SUPERVISORS:
Mr. V. Venus
Dr. Ir. C. van der Tol

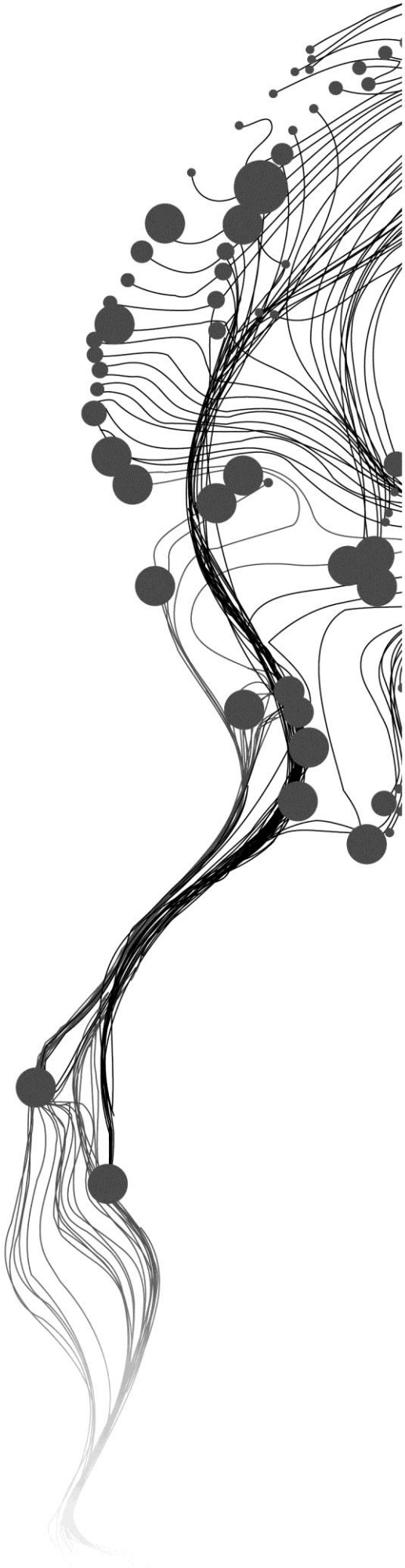

UNDERSTANDING URBAN HEAT ISLAND BY ASSESSING LAND SURFACE TEMPERATURE AND SURFACE PARAMETERS ACROSS DIFFERENT BUILT-UP CLASSES

BADAL KUMAR DASH
Enschede, The Netherlands, June, 2015

Thesis submitted to the Faculty of Geo-Information Science and Earth Observation of the University of Twente in partial fulfilment of the requirements for the degree of Master of Science in Geo-information Science and Earth Observation.
Specialization: Geo-information Science and Earth Observation for Environmental Modelling and Management

SUPERVISORS:
Mr. V. Venus
Dr. Ir. C. van der Tol

THESIS ASSESSMENT BOARD:
Prof. Dr. A.K, Skidmore (Chair)
Ben Sonneveld (External Examiner, Centre for World Food Studies)
Mr. V. Venus
Dr. Ir. C. van der Tol

ABSTRACT

The surface urban heat island which forms at the urban surface is investigated through the distribution of Land Surface Temperature (LST). Urban surface is comparatively hotter during the day time with the presence of sun radiation, which can be estimated by LST. The distribution of LST in the Enschede Municipality area is examined with a detail Built-up land use map for a clear-sky summer day. The influence of land surface parameters *i.e.,* surface emissivity, broadband surface albedo, and, satellite derived vegetation abundance (NDVI) and Built-up density (NDBI) indices on LST is also investigated. The LST and land surface parameters were retrieved and derived from an ASTER image which was acquired at 31th May, 2003. This study is also focused on how LST varies with the variation of land surface parameters through a multivariate linear regression model. The first objective is to test whether LSTs are significantly different across different Built-up land use classes in the urban area and, to identify which classes are significantly different from others. Subsequently, a thermal map of the study area is generated by reclassifying built-up classes according to LST as indicator. This thermal map of a city might be useful to identify the hotter/cooler areas and to find a solution to mitigate heat island effects accordingly. The second objective is to investigate the relationship between LST and land surface parameters through visual interpretations, quantitative analysis and multivariate regression analysis. Result suggests that LST have a positive correlation with NDBI, and a negative correlation with NDVI and emissivity. A weak relationship is found with albedo. The multivariate linear regression model suggests only 23.7 per cent variance of LST can be explained by the model. However, hypothesis test found the relationship is statistically significant and the residuals are normally distributed indicates model might be useful to predict LST. Furthermore, the NDBI appeared as the most influential regressor in shared covariance analysis. NDBI together with NDVI and emissivity explains about 97 per cent of the model variance.

Keywords: Surface Urban Heat Island, LST, Built-up, Albedo, NDBI, Atmospheric correction

ACKNOWLEDGEMENTS

I would like to thank my supervisors, Mr. V. Venus and Dr. Ir. C. van der Tol, for all constructive comments and suggestions.

I would thank my sponsor the Joint Japan/World Bank Graduate Scholarship Program (JJ/WBGSP) for the providing the opportunity.

I would also like to extend my deepest gratitude to my friends and family for their constant moral support and love.

TABLE OF CONTENTS

LIST OF FIGURES

LIST OF TABLES

1. INTRODUCTION

1.1. General Introduction

The impacts of urbanization on climate at all scales are the main concern of urban climate research. Urbanization impacts the urban environment mainly by population, covering urban surface, and changing in physical properties and chemical concentration of atmosphere. The cumulative effect from all these is called as urban heat island effects, simply define as a man-made area which is significantly warmer than its surrounding countryside. It is usually measured by the term urban heat island intensity, which is define as the difference between maximum urban temperature and the background rural temperature (Oke, 1988). This phenomenon was first investigated by Luke Howard (Mills, 2007), whose research was on the climate of London represents the beginning of the field in the 1810s. The heat island exists because the land surface in urban areas absorbs heat from sun and stores the heat. That is also coupled with concentrated energy consumption and less ventilation than rural areas. As a result a 'warm island' in 'cool sea' is formed. The temperature difference is usually larger at night than day time, stronger with weak wind and most noticeable during summer and winter. There are two types of heat island: (1) Atmospheric Urban Heat Island - forms at air, and measures by weather stations and mobile transverses. (2) Surface Urban Heat Island - forms at surface, most noticeable at daytime and, typically characterized as a measurement of Land Surface Temperature (LST) based on the use of thermal remote sensing. The adverse effects of Urban Heat Island (UHI) are significant. It deteriorates living environment, increases energy consumption, elevates emissions of air pollutants and greenhouse gases, impairs water quality, compromises human health and comfort, and even increases mortality rate (Akbari *et al.*, 2008; Rizwan *et al.,* 2008). Due to adverse environmental and economic impacts on society, heat island determination and mitigation research draws more attention of urban climate researchers and engineers. Assessment of urban heat island varies from research approaches and applied measurement techniques (Arnfield, 2003; Grimmond, 2005; Rizwan *et al.*, 2008).

1.2. Problem Statement

According to the Global Health Observatory (GHO) data from World Health Organization (WHO), the urban population in 2014 accounted for 54% of the total global population and the trend is expected to grow approximately 1.84% per year between 2015 and 2020 (GHO, 2014). The rapid increase in urbanization influences urban thermal environment which is closely related to energy consumption, human health and comfort.

The conversion of natural green surfaces to non-evaporative and impervious surfaces leads to increase in sensible heat. Urban materials such as concrete masses, asphalt roads and metal surfaces exhibit a high degree of thermal inertia. These materials are characterized by high heat capacity and low solar reflectivity. Such urban surface materials can cause a reduction in potential cooling rate as compare to natural surfaces (Akbari *et al.,* 2008). Also, an expansion of built-up surface tends to reduce natural surface that, leads to a possible decrease in overall vegetation.

Conceptually, the thermal emitted radiance from any surface depends on following factors:

- The surface temperature, which is an indication of thermodynamic state resulting from the energy balance between surface and atmosphere (Mallick, Kant, & Bharath *et al.*, 2009).
- The surface emissivity, which is the efficiency of the surface for emitting radiant energy, depends on the composition of surface, surface roughness etc.

- Surface albedo, which is the fraction of the incoming solar radiation that is reflected by the surface

These three parameters play a key role in the estimation of the energy budget of the surface. Therefore, Land Surface Temperature (LST) is considered to be a reliable indicator of UHI as there is generally a close correlation between LST and near-surface air temperature. On the other hand, the remote sensing approach appears to be very attractive for the assessment of LST. Land surface parameters like surface emissivity, surface albedo etc., and other biophysical parameters which have influences on UHI are also possible to derive quantitatively by remote sensing approach. Thus, this study is mainly focused on (1) the impact of different urban surfaces on Urban Heat Island (UHI) by investigating the distribution of Land Surface Temperature (LST) across different built-up classes and, (2) estimating relationships between LST and land surface parameters derived by remote sensing technique from a city.

1.2.1. Research Motivation and Scope

Research showed that the existence of urban heat island in European cities and its intensity is also noticeable (Grimmond, 2005). The heat island studies were also performed in Dutch cities from last decade after two extreme hot summers at heat-wave year 2003 and 2006. Van Hove *et al.,* (2011) assessed the heat island intensity and future trends for the Netherlands based on the results of previous studies reported in literature. They found that maximum intensity for Dutch cities are substantial and of the same magnitude of those found in other European cities. From their report it is clear that heat island will become a critical issue in the next decades especially in the western of part of the country. The heat island effect is also found in a Dutch city like Enschede from investigation by ITC researchers (van der Tol, pers. comm.). However, the spatial distributions of heat island intensity across various built-up types for Dutch cities are still unclear. A lack of urban climate studies with the use of satellite data might be a probable cause of it. So far, most noticeable researches that were conducted in Dutch cities are either only based on station data or a combination of airborne and station measurements. Steeneveld *et al.,* (2011) applied *in situ* measurements with meteorological station data, and Brandsma *et al.,* (2003) mainly used meteorological station data for a city to quantify the UHI for a group of cities in the Netherlands.

Due to a high spatial coverage and opportunity to estimate various surface parameters from satellite observations, a study on spatial variation of land surface temperature across different built-up types is possible. Exploring the satellite derived explanatory variables of LST is important for mitigation planning. In the present study emphasis has been to estimate Land surface Temperature (LST), surface emissivity, broadband surface albedo, and sensor derived indicator of vegetation abundance (NDVI) and, indicator of built-up information (NDBI) etc. from ASTER sensors attached in TERRA satellite.

1.2.2. Assumptions and limitations of the present study

One assumption for this study is that the micro-meteorological conditions (air temperature, wind, humidity etc.) only slightly affect radiative temperature. Micro-meteorological differences within the study area are not significantly impacting the land-surface temperature. We therefore assume that LST differences, e.g. caused by sunlight vs. shadow-sided parts of the urban environment, are uncoupled from the atmosphere, i.e., the air above. This assumption is claimed from Beta Paramitaa, (2012) reported results of ENVI-Met model by comparing two building groups based on the orientation in the urban area Fukuoka, Japan and found that air temperature does vary slightly from sunlit to shaded part of the particular group of building. They found that, Tmrt (mean radiant temperature) reach 71.8ºC for the sunlit part of the open space and about 35.87-46.30ºC for the shaded area. In contrast, Ta (air temperature) for sunlit part of open space reaches 32.29-33.15 ºC and 32.29-33.54 ºC for shaded area. Parlow *et al.,* (2014) reported that during daytime when satellite thermal infrared imagery shows increased surface temperatures in the city, the air temperature differences (urban and rural) over the whole year are very low and range from + 0.25 to + 0.5 K.

Furthermore, the spatial resolution of a far-thermal infrared (FTIR) observation from a space-borne sensor such as ASTER is generally coarser then individual built-up elements (hor. resolution of an image element ≈ 90m at nadir). Since micro-meteorological phenomena are not commensurate with the scale of space-borne thermal observation one would hard pressed to model and quantify their interaction.

In contrary, this FTIR spatial resolution is assuming sufficient to detect spatial variations in LST at individual built-up class (topographic settings of urban area) scale.

Another assumption is the spatial characteristics of surface temperature are contingent upon the configuration and topographic setting of the urban area. A sketch of a typical UHI profile in Figure1.1 shows how surface temperature varies over different built-up classes in the urban area. This profile also indicates the variation of surface and air temperature is not constant. The spatial distribution of surface temperature is more related to land surface parameters and configuration of different built-up classes than the distribution of air temperature.

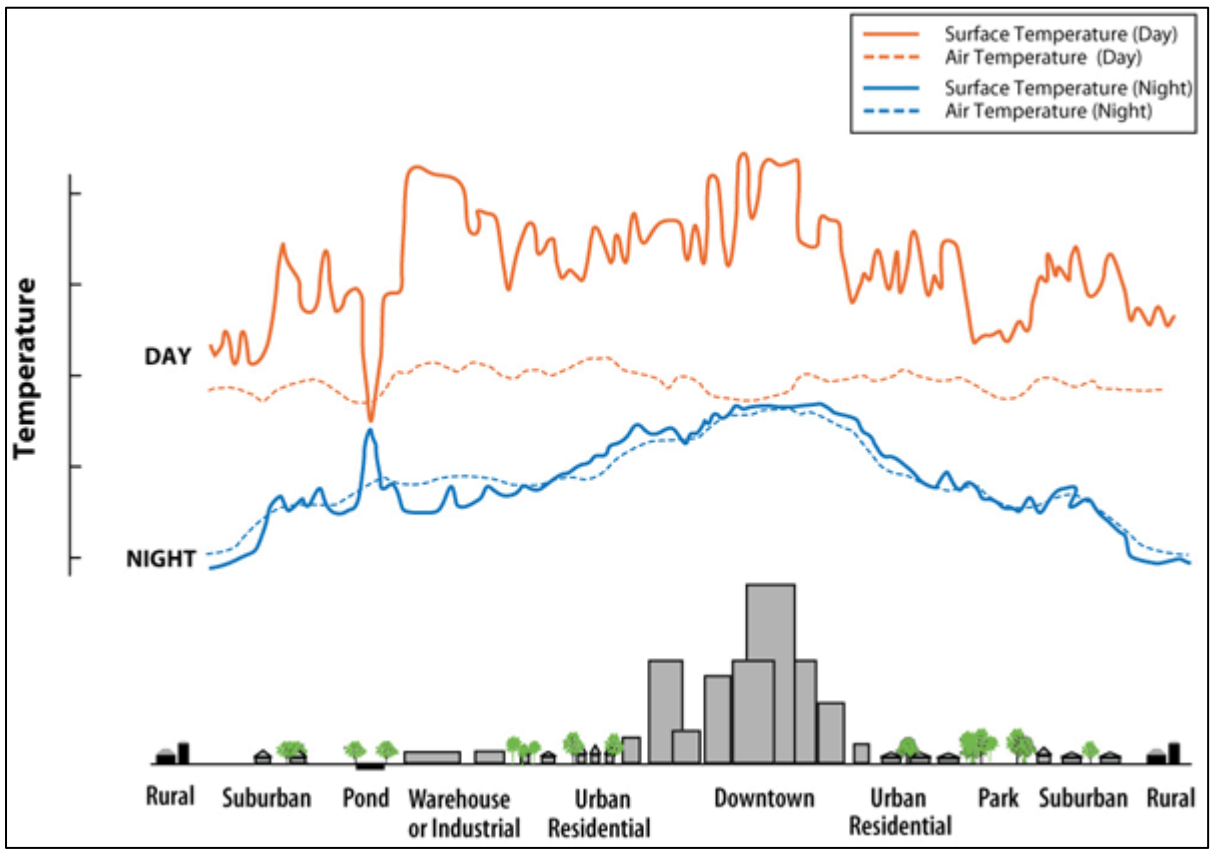

Figure 1.1 The variations of air and surface temperature across different built-up areas. Source: EPA 2008, (Akbari *et al.,* 2008).

1.3. Research Objectives , Research Questions and Hypothesis

1.3.1. General Objectives

The overall objective of this study is to investigate the impacts of different built-up classes on surface urban heat island effect (Land Surface Temperature (LST)) in Enschede, the Netherlands, and the relationship between LST and selected land surface parameters using remote sensing techniques.

In order to achieve the main research objective the following specific objectives are set for the study:

1.3.1.1. Specific objective 1 and corresponding research questions and hypothesis

Specific objective 1:

To study the distributions of LST across built-up classes for a summer day image

Research questions to objective 1:

Are the LST significantly different across different built-up classes? And which pairs of built-up classes are significantly different, therefore, one is significantly warmer than the other (s)? What is the order of built-up classes in terms of LST?

Hypothesis Test 1: (Kruskal-Wallis Test and Tukey post hoc rank test to compare all possible pairs)

Null Hypothesis – Mean rank of LST of each built-up class is the same.

$$H0; \mu_{LST}1 = \mu_{LST}\,2 = \mu_{LST}\,3 = \mu_{LST}4 = \mu_{LST}\,5 = \mu_{LST}\,6 = \mu_{LST}\,7$$

Alternative Hypothesis – Mean rank of LST of different built-up classes can be ordered as warmest to the coolest.

$$HA; \mu_{LST}1 > \mu_{LST}\,2 > \mu_{LST}\,3 > \mu_{LST}\,4 > \mu_{LST}\,5 > \mu_{LST}\,6 > \mu_{LST}\,7$$

(Built-up classes: 1= Factory areas, 2 = Road surfaces, 3= High-rise Residential, 4= Low-rise Residential, 5 = City centre, 6 = other mixed area and, 7 = Park).

1.3.1.2. Specific objective 2 and corresponding research questions and hypothesis

Specific objective 2:

To study the distributions of emissivity across build-up classes for a summer day image

Research questions to specific objective 2

Are the emissivities significantly different across different built-up classes? And which pairs of built-up class are significantly different, therefore, one is significantly warmer than the other (s)? What is the order of t-up classes in terms of emissivity?

Hypothesis Test 2: (Kruskal-Wallis Test and Tukey post hoc rank test to compare all possible pairs)

Null Hypothesis: Mean rank of emissivity of each built-up class is the same.

$$H0; \mu_e 1 = \mu_e\,2 = \mu_3\,3 = \mu_e 4 = \mu_e\,5 = \mu_e\,6 = \mu_e\,7$$

Alternative Hypothesis – Mean rank of emissivity of different built-up classes can be ordered as lowest to highest.

$$HA; \mu_e 1 < \mu_e\,2 < \mu_e\,3 < \mu_e\,4 < \mu_e\,5 < \mu_e\,6 < \mu_e\,7$$

(Built-up classes: 1= Factory areas, 2 = Road surfaces, 3= High-rise Residential, 4= Low-rise Residential, 5 = City centre, 6 = other mixed area and, 7 = Park).

1.3.1.3. Specific objective 3 and corresponding research questions and hypothesis

Specific objective 3:

To build a multiple regression linear model of LST from surface broadband albedo, surface emissivity, NDVI and, normalized Build-up Index (NDBI).

$$LST = b_0 + b_1(\alpha) + b_2(\varepsilon) + b_3(NDVI) + b_4(NDBI) + \varepsilon'$$

$$Here, b_0 \text{ is the intercept}, b_1, b_2, b_3, b_4 \text{ are regression coefficients and } \varepsilon' \text{ is error}$$

Research question to objective 3:

Is the model statistically significant at 95 % confidence level? How much variation (assessed from the model's coefficient of determination, R^2) in LST can be explained by the model?

Hypothesis Test 3: (Regression model)

Null Hypothesis – The overall model is not statistically significant at 95% of confidence level (all regression coefficients are zero, *i.e.,* none of the regressors contribute significantly to the prediction of LST).

Alternative Hypothesis – The overall model is statistically significant at 90% of confidence level (at least one regression coefficient is significantly different from zero *i.e.,* at least one regressor contributes significantly to the prediction of LST).

1.4. Theoritical Background

1.4.1. Urban Surface Energy Balance

The Surface Energy Budgets (SEB) of urban areas is different from those of surroundings. The differences in urban and rural surface characteristics and land cover types affect heat generation and transfer. Oke (1988) describes the urban thermal behaviour and gave a comprehensive review of energy balance approach and its development as applied to urban areas. If the net horizontal heat advection is not considered, the SEB for an urban area can be expressed (Weng, 2009) as

$$R_n + A = H + LE + G \ \ (Wm^{-2}) \quad \text{----------(eq1)}$$

where:
R_n is the net all wave radiation,
A is anthropogenic heat discharge,
H the sensible heat flux,
LE the latent heat flux, and;
G the net storage heat flux associated with heating/cooling of this air mass.

So, in principle, urban climate is driven by urban SEB and radiation balance. Each energy balance component (Figure 1.2) can be altered in urban environment and contribute to the generation of the UHI effects. Compared to the vegetation and other natural ground cover, urban surfaces, absorbs more radiation and reflects less radiation back to the atmosphere. The thermal properties of surface cover materials, as well as, urban geometry leads to lower solar reflectance of urban surfaces. For example, building walls can cause to reflect some short-wave radiation to the surfaces rather than being sent back to

the atmosphere. Similarly, the urban structure can obstruct the release of long-wave radiation to atmosphere at night. Particularly, densely built areas with a low sky view factor cannot easily release long-wave radiation to atmosphere, causes heat trapped and drives to the urban heat island (Van Hove *et al.,* 2011). Due to relatively low soil moisture in the urban surface, urban areas trends to have less evapotranspiration (ET) compared to natural landscapes. The individual components of heat balance and how the LST is the integral part of individual components are described below.

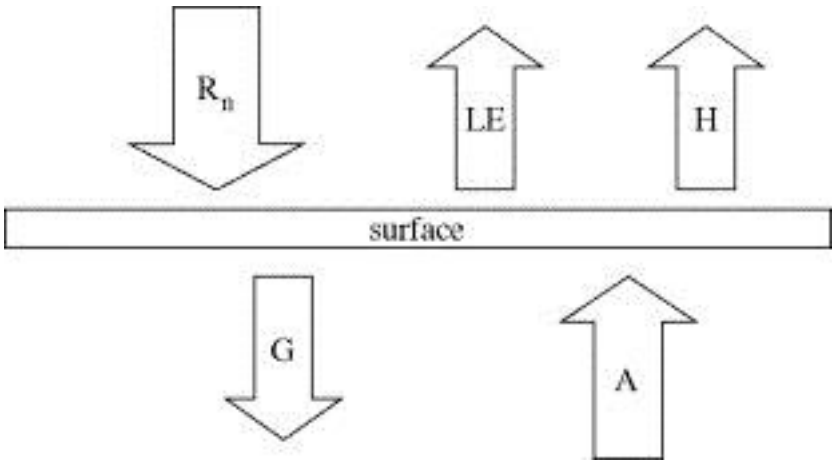

Figure 1.2 A schematic diagram of heat balance at urban land surface. Rn: net radiation, A: anthropogenic heat discharge, G: ground heat flux, LE: latent heat flux, H : sensible heat flux. source: (Kato & Yamaguchi, 2007)

1.4.1.1. Net Radiation, R_n

The formula to calculate the net radiation is given by:

$$R_n = (1-\alpha)R_{swd} + \varepsilon R_{lwd} - \varepsilon\sigma T_0^4 \text{ ---------- (eq2)}$$

where *a* is the surface reflectance (albedo) related to land surface types*,* R_{swd} is the downward short wave radiation measured at the weather station*,* R_{lwd} is the downward long-wave radiation, ε is the emissivity of the surface, σ is the Stefan– Boltzmann constant, and T_0 is the surface temperature. *a*, ε, and T_0 can be derived from remote-sensing data.

Downward long-wave radiation, $R_{lwd} = \varepsilon_a \sigma T_a^4$ ---------- (eq3)

ε_a = emissivity of the atmosphere = $9.2 * 10^{-6}(T_a + 273.15)^2$; -------- (eq4)

Ta = air temperature at reference height.

The net radiation is affected by relative contribution of direct vs. defuse radiation during summer and winter time. The winter generally characterize by defuse sunlight due to increased cloudiness, that changes the net radiation significantly.

1.4.1.2. Ground heat flux, G

Measured by parameterizing as a constant fraction of net radiation as

$G = c_g R_n$; ---------- (eq5)

c_g= fixed coefficient to surface type

The value of c_g depends on the heat capacity and heat conductivity of surface materials. A high heat capacity results in a low c_g, and high heat conductivity results in a high c_g. The opposite relationships are

also true. The surface materials of developed areas (i.e., concrete and asphalt pavement) generally have both higher heat capacities and higher conductivities than soil or vegetation.

1.4.1.3. Sensible heat flux, H

Convection describes the transfer of sensible heat flux that we feel as temperature between surface and air. It can be expressed as,

$$H = \frac{\rho_a C_p (T_0 - T_a)}{r_{ah}} \quad \text{---------- (eq6)}$$

T_a is the air temperature measured at ground , T_0 is surface temperature inferred from satellite, r_{ah} is the aerodynamic resistance (sm^{-1}) to heat transport, generally calculated from wind speed, height at which the wind speed is measure, roughness lengths for momentum and heat transport. The aerodynamic resistance values for urban area can be estimated from several empirical equations. The detail description of estimating r_{ah} can be found in Kato & Yamaguchi (2005); Zhang, Balzter, & Wu (2013).

Since, the combined T_0 & T_a measurements for each land unit need to be measured at the same time, there is a practical problem in combining T_0 & T_a measurements to estimate ($T_0 - T_a$). Therefore, ($T_0 - T_a$) can be estimated from an inversion of the transfer equation (Youshui Zhang *et al.,* 2013) for sensible heat flux.

$$T_0 - T_a = \frac{H r_{ah}}{\rho_a c_p} \quad \text{---------- (eq7)}$$

Here, H is only known at the extremes of T_0. For coldest pixel, H=0 and H=R_n – G, for the warmest pixels. $T_0 - T_a = 0$ is linked to low-sensible heat flux and a high value of ($T_0 - T_a$) coincided with high- sensible heat flux. Therefore, T_0 can be used to interpret $T_0 - T_a$ across the image using following regression equation (Youshui Zhang *et al.*, 2013),

$$T_0 - T_a = a\,T_0 - b \quad \text{---------- (eq8)}$$

Where a and b are the linear regression coefficients valid for one particular moment in time and a specific landscape. The minimum and maximum values of $T_0 - T_a$ can be calculated for the coldest and warmest pixels, and *a* and *b* are calculated based on these pixels with given H, $T_0 - T_a$, and T_0 values.

1.4.1.4. Latent heat flux, LE

Evapotranspiration describes the transfer of latent heat from earth surface to air via evaporating water. The urban surface trends to have less evapotranspiration than natural landscape. The impervious urban surface leads to very high surface temperatures. LE from impervious surface can be estimated by satellite is usually assumed to be zero. LE for urban area can be estimated from the portion to fractional vegetation cover (FVC) in every image pixel of the urban area (Youshui Zhang *et al.*, 2013).

1.4.1.5. Anthropogenic heat, A

The sources of this term of heat flux are heat generated by motor vehicles, air conditioners, industrial facilities and other man-made sources usually, estimated from the residual of energy balance in the urban area. The average amount of anthropogenic release over a city is usually less than 100 w/m^2 (Grimmond, 2005). The amount of anthropogenic release may not be directly measureable, rather estimating by isolating it from other terms in the energy balance equation. As a result, accuracy of this estimation is uncertainty, since the uncertainty to noise of individual term might be cumulative and total noise is equally large as the magnitude of the A.

1.4.2. Land surface temperature

Land Surface Temperature (LST) is an important parameter in the studies of urban thermal environment and dynamics. It is important in determining some components of energy balance equation. Remotely sensed thermal infrared (TIR) data have contributed to address the urban heat island through the estimation of LST. A series of satellite and airborne sensors have been provided Thermal Infrared (TIR) data from the Earth surface, such as Landsat TM/ETM+, AVHRR, MODIS, ASTER, and TIMS. These TIR data have widely used to retrieve LST. In addition to LST, these TIR sensors may also be utilized to obtain emissivity data of different surfaces with various resolutions and accuracies (Mitraka *et al.*, 2012). LST is a primary factor in determining surface radiation and energy exchange. The spatial distribution of LST is governed by surface heat fluxes obviously affected by urbanization(Qin *et al.*, 2006; Sun & Yu, 2013). Increasing urbanization and industrialization has caused changes in the heat balance in densely built urban areas. In such cases LST in urban area is usually higher than the temperatures of the surroundings. LST and emissivity data are used in urban climate and environmental studies, mainly for analysing LST patterns and its relationship with surface characteristics, for assessing urban heat island (Weng, Lu, & Schubring, 2004). Moreover, landscape properties, patterns, and processes can be characterized from LST relation with surface energy fluxes (Weng, Liu, & Lu, 2007). The physical properties of various types of urban surfaces and urban geometry are important factors that determine LST in a city (Voogt & Oke, 2003).

1.4.3. Thermal and optical properties of materials for the urban environments

The characteristics of the materials used in urban environments influence urban heat island development, as they determine how the sun energy is reflected, emitted, and absorbed. In particular, *the optical characteristics of materials especially the albedo to solar radiation and emissivity to long-wave radiation,* have a very important impact on the urban energy balance (Asimakopoulos *et al.*, 2011). The solar energy reaching the earth in different percentages: 5 per cent of solar energy is in the ultra violet spectrum; 43 per cent is visible light; and the remaining 52 per cent of solar energy is infrared, felt as heat (Akbari *et al.*, 2008).

The albedo is the percentage of solar energy reflected by the surface. It is correlated with the material's color due to visible spectrum of solar energy. Darker surfaces are likely to have lower albedo values than lighter surfaces. Structures built with low albedo materials reflect less and absorbed more of the sun's energy. As a result, surface temperature increases in the urban area. The use of high albedo materials reduces the amount of solar radiation absorbed through building's walls, roofs and pavements thus keep surfaces cooler. Asimakopoulos *et al.,* (2011) listed the albedo of various typical materials and areas (in Table 1.1); the albedo and emissivity for selected materials (in Table 1.2) that those were reported in different articles. However, measured values for albedo and emissivity are not available for most urban locations. Offerle, Grimmond, & Oke (2003) estimated surface albedo and emissivity for Chicago and LA, USA, in order to study net all-wave radiation of those cities. They used site characteristics like dominant surface cover, percentage of vegetation and materials used in urban infrastructures as well as values taken from literature. Their used values of albedo and emissivity of different urban surfaces are given in Table 1.3. The thermal emittance or emissivity of a material *(emissivity refers to a material property (of a homogeneous material), while emittivity refers to specific samples or objects)* also play important role in urban environments. Materials emit long-wave (infrared) radiation which is the function of emissivity of the materials and its temperature. Surface with high emittance values will stay cooler, because they will readily release the energy that has been absorbed as short-wave radiation. Although solar reflectance and material's emissivity are the main determinant of surface temperature, material's heat capacity- its ability to store heat,

determine the temperature of a material. Urban infrastructure are typically more effective at storing heat due to the use of higher heat capacity materials than rural (Akbari *et al.*, 2008). Christen & Vogt (2004) reported that a downtown area of a metropolitan city can store twice amount of heat than its rural surroundings. Buildings in the urban acting differently on the net radiation balance since they exhibit differently in different thermal behaviour. Thermal and optical properties of materials used in different built-up structure influence LST in the urban area.

Table 1.1 Albedo of typical urban materials and areas (adopted from Asimakopoulos *et al.,* (2011))

Surface	**Material**	**Albedo**
Streets	Asphalts	0.05 – 0.2
Walls	Concrete	0.10 – 0.35
	Brick/stone	0.20 – 0.40
	Whitewashed stone	0.80
Roofs	Asphalt	0.10 – 0.15
	Tar and gravel	0.08 – 0.18
	Tile	0.10 – 0.35
	Highly reflecting roof after weathering	0.6 – 0.7
Paints	White	0.50 – 0.90
	Red, brown, green	0.20 – 0.35
	Black	0.02 – 0.15
Urban areas		0.10 – 0.27 (average: 0.15)
Others	Artificial turf	0.10 – 0.50
	Average soil	0.30
	Dry sand	0.20 – 0.30
	Deciduous forests	0.15 – 0.20
	Coniferous forests	0.10 – 0.15
	Wood (oak)	0.10
	Grass	0.05

Table 1.2 Albedo and emissivity for selected surfaces (adopted from Asimakopoulos *et al.,* (2011))

Material	**Albedo**	**Emissivity**
Concrete	0.3	0.94
Red brick	0.3	0.90
Building brick	-	0.45
Concrete tiles	-	0.63
Wood (freshly planted)	0.4	0.90
Tar paper	0.05	0.93
White plaster	0.93	0.91
Bright galvanized iron	0.35	0.13
Bright aluminum foil	0.85	0.04
Gravel	0.72	0.28
sand	0.24	0.76

Table 1.3 Albedo and emissivity for selected surfaces and corresponding fractional area of the city estimated by Offerle, Grimmond, & Oke (2003) for cities Chicago and LA, USA.

Urban surface	Plan area fraction	Albedo	Emissivity
Roof	0.32	0.06	0.92
Wall	-	0.15	0.90
Road	0.38	0.11	0.94

1.4.4. Normalized indices of vegetation and built-up cover

The Normalized Difference Vegetation Index (NDVI) is one of the most widely applied vegetation indices to strengthen the vegetation information. On the other hand, Normalized Difference Build-up Index (NDBI) is used to strengthen building information (Liu & Zhang, 2011). Both indices are derived from optical bands of ASTER image.

1.5. Literature Review

Researches related to urban climate can roughly be categorized into three divisions considering measurement techniques and approach of analysis.

1.5.1. Physical and empirical studies from observational networks or *in situ* measurements

Oke (1981) first modeled urban heat island by explaining surface energy balance for urban form observations. The heat island intensity, spatial and vertical structure and dynamics were also reviewed by him. Mills (2007) describes his work as "synonymous with the modern history of urban climate research". The method of describing UHI is not differing significantly from his work to present (Arnfield, 2003). The parameters related to urban land surface energy flux are mostly measured in the traditional way in the network of meteorological stations or *in situ* field measurements and then estimates from statistical fit. Similar empirical methods was also applied by Brandsma, Konnen, & Wessels (2003) at De Bilt, Netherlands; Lee & Baik (2010) at Seoul, South Korea; Borbora & Das (2014) at Guwahati, India; Busato, Lazzarin, & Noro (2014) at Padua, Italy; Lokoshchenko (2014) at Moscow for heat island studies.

1.5.2. Remote sensing of urban climate studies

A major portion of recent urban heat island studies was done using combination of energy balance and remote sensing techniques. Land surface temperature (LST) retrieved from Thermal Infrared (TIR) remotely sensed data have been widely used for assessing urban heat island (Weng, 2009). LST is an important factor for the determination of many biophysical parameters and processes. It enables monitoring of surface energy fluxes, particularly evapotranspiration (Gowda *et al.*, 2008; Tang & Li, 2014; Tian *et al.*, 2012; Tol & Parodi, 2012), crop production (Holzman *et al.*, 2011) near surface air temperature (Zakšek & Oštir, 2012) etc. The urban climate studies using LST was also carried out extensively by Jin, Dickinson, & Zhang (2005); Lee & Ho (2010); Offerle, Grimmond, & Oke (2003); Zakšek & Oštir (2012); Zhang *et al.,* (2013); Kato & Yamaguchi (2005 & 2007) for estimating urban surface energy fluxes. The spatial and temporal variation of urban surface temperature have been investigated by Anniballe, Bonafoni, & Pichierri (2014); Qiao, Tian, & Xiao (2013); Weng, Lu, & Schubring (2004); Xiao *et al.,* (2008). The relationship between LST patterns and land cover type have been investigated by Anniballe, Bonafoni, & Pichierri (2014); Chen, Zhao, Li, & Yin (2006); Essa *et al.,* (2013); Qiao, Tian, & Xiao (2013); Weng, Liu, & Lu (2007) at different urban areas of World. These studies was also based on different TIR sensors from ASTER, MODIS, AVHRR for LST and different OLI sensors from Landsat, MODIS, CORINE for land use land cover (LULC). In most cases they found a good correlation between LST

variation and LULC changes, which is a good indicator of patterns of UHI with LULC changes. To simulate urban LST distributions, some physical based and numerical models have been developed. Oke (1988) and Voogt & Oke (1997) developed urban energy balance model, Streutker (2002) proposed a Gaussian model. Among these models statistical analysis plays an important role incorporating LST to the urban surface characteristics and linking LST with biophysical and meteorological factors which have influence on urban climate (Bottyán *et al.*, 2005). The relationship between LST and other land surface parameters such as: vegetation abundance, land use types, surface albedo, and material's emissivity were further investigated by Bottyán *et al.,* (2005); Chrysoulakis *et al.*, 2014; Jin *et al.,* (2005); Lee, Choi, & Lee (2014); Ryu & Baik (2012); Wang *et al.,* (2007); Weng *et al.,* (2004); Weng & Lu (2008); Yuan & Bauer (2007).

1.5.3. Studies on properties of urban materials and relation to urban temperature

The thermal and optical performance of materials and their impacts on the urban climate has been studied widely in the past. Yap (1975) found that differences in urban-rural surface emissivity are the potential cause of heat island effect. Asimakopoulos *et al.,* (2011) found that LST is significantly different in different build-up structure. They measured the distribution of surface temperature of pavements and roads in seven different canyons in Athens, Greece and reported that relative temperature of asphalt is 63^0 C, white pavements close to 45^0 C and over grass is close to 38^0 C. They also noticed that lower surface temperature tends to decrease the ambient air temperature, which has a significant impact on energy consumption in the urban. On the other hand, Oke (1988) studied the effect of thermal and optical performance of materials used to the heat island intensity during night and found an increase of emissivity from 0.85 to 1.0, there was a slight increase of 0.4 K in urban-rural temperature difference for very tight canyons, while there was almost no change for higher view factors. In contrast, thermal properties of material (thermal admittance) used to be more important, a decrease of thermal admittance of 600 $J/m^2/k$ in the urban area, heat island intensity may be decrease up to 4 k. The albedo and surface temperatures of material used in urban were measured by Taha, Sailor, & Akbari (1992) and found that white coating with an albedo of 0.72 was 45k cooler than black coating with an albedo 0.08 in the early afternoon of a summer day. They also reported that white surface (albedo= 0.61) was only 5k warmer than ambient air, in contrast, gravel surface (albedo= 0.09) was 30k warmer than air (Taha, 1997). The spatial distribution and seasonal variation of surface albedo in a heterogeneous urban landscape was examined by Brest (1987) from Landsat observation. He noticed the key factors of determining albedo and its seasonal dynamics are vegetation abundance and canopy structure. Thus the role of albedo is important in formation of urban heat island.

2. DATA AND METHODS

This Chapter describes the data used in the analysis and outlines all data pre-processing, preparation and processing methods performed in the study. ESRI ArcGIS™ 9.3 and ILWIS 3.8.4.0 (Integrated Land and Water Information System) software were employed to complete all the procedures summarized in this chapter.

2.1. Study Area

With over 158,000 inhabitants (Statline, 2015), Enschede is the largest city in the eastern Netherlands in the province of Overijssel and in the Twente region. The area of the municipality is 142.72km^2 with water of 1.72 km^2. According to the Köppen classification, Enschede features an oceanic climate (Cfb), like most of the Netherlands. KNMI observed daily mean temperature and average precipitation in the Twenthe region is shown in Table 2.1.

Table 2.1 Climate data for Twenthe : Long-term averages(1981-2010). Source: (KDC), KNMI

Month	Jan	Feb	Mar	Apr	May	Jun	Jul	Aug	Sep	Oct	Nov	Dec	Year
Daily Mean (°C)	2.3	2.6	5.6	8.9	12.9	15.4	17.6	17.1	14.0	10.2	6.0	2.9	9.63
Average PP (mm)	71.5	51.6	65.1	45.2	62.4	67.7	74.5	71.0	65.4	67.5	68.8	74.1	784.9

2.2. Data

2.2.1. Land Use data

A dataset depicting Land Use and land Cover (LULC) over Enschede Municipality area was used for this study. A collection of digital Topographic maps (for the whole of The Netherlands) entitled "TOP10NL (BRT)" used to prepare a land use map and a detail Built-up map over the study area. The data provided by the Dutch Kadaster as geodatabase updated till November, 2012. TOP10NL is the most detail digital nationwide topographic data at scales between 1:5,000 and 1:25,000, originated from aerial photographs, field recordings and information from external files. It is made of different topographic features with the following classes: (source: TOP10NL metadata and websites)

- road section,
- railway section,
- water portion,
- building,
- grounds,
- design element,
- relief,
- registrative area,
- geographical area
- functional area.

2.2.2. Satellite Image

The ASTER (Advanced Spaceborne Thermal Emission and Reflection Radiometer) sensor is an imaging instrument flown on the Terra satellite which was launched in December 1999. The Terra spacecraft is flying in a circular, sun-synchronous orbit at an altitude of 705 km, returning to the same orbit every 16 days. ASTER has been designed to acquire land surface temperature, emisivity, reflectance, and elevation data and is a cooperative effort between NASA and the Japanese Ministry of Economy, Trade, and Industry (METI). An ASTER scene covers an area of approximately 60 km by 60 km and data is acquired simultaneously at three resolutions. The images are georeferenced to the WGS-84 datum and Universal Transverse Mercator projection. The scenes are normally delivered in the along-track orientation to produce a smaller dataset. The primary full ASTER dataset is the ASTER L1B Registered Radiance at the Sensor product. This complete ASTER scene consists of 14 bands of data (Table 2.2); including one band (3B) which points backwards to create parallax. Also note that at-sensor radiance values have been scaled to integer digital numbers (DNs). The products are stored and distribute in the form of Hierarchical Data Format called HDF-EOS.

Table 2.2 ASTER Instrument characteristics

Wavelength region	Band No.	Spectral Range (μm)	Ground Resolution, m	Swath Width (km)
VNIR	1	0.52-0.60	15	60
	2	0.63-0.69		
	3N	0.78-0.86		
	3B	0.78-0.86		
SWIR	4	1.60-1.70	30	
	5	2.145-2.185		
	6	2.185-2.225		
	7	2.235-2.285		
	8	2.295-2.365		
	9	2.360-2.430		
TIR	10	8.125-8-475	90	
	11	8.475-8.825		
	12	8.925-9.275		
	13	10.25-10.95		
	14	10.95-11.65		

ASTER image acquired on 31th May, 2003 is used to derive LST, albedo, emissivity, NDVI and NDBI over the study area. The image collected from ITC data server (geo data warehouse) was originally distributed by LP-DAAC (Land Processes Distributed Active Archive Center). The image was captured at 12:45 CEST (10:45 UTC) time under clear atmospheric conditions (0%) cloud coverage. required additional information that used in image pre-processing is attached in the Appendix-A.

2.3. Land Use Data Preparation

The TOP10NL dataset contains different topographic features. Terrain data is used to prepare a Land Use map with 5 major classes. The given nomenclature of classes were tried to keep the same as it found in the original data. However, two or more classes were dissolved to a new one and named after the dominant one. For example, the "Forest and grassland" class was a collection of different type forests and grassland. Table 2.3 shows the area of each Land use with their class name. The main concern with the Land Use map preparation was to keep non-natural surfaces separate from natural one and to see whether they exhibit different characters in the analysis. In the final Landuse map

Forrest/grassland is the dominant and water body is the least dominant class. Few areas in the data were found whose surface type was unclear (vegetated/non-vegetated), was excluded from the classification and will appear as white color (not define) in the Landuse map. The land use map is shown in the Figure 2.1 (bottom map) and the location of study area with an ASTER image (60 *60 km) as background (top map).

Table 2.3 LandUse type and corresponding area in the study area

Zone code	LU Type	Area (km²)
0	Built-up	8.44
1	Rail and road surface	11.15
2	Cropland	14.08
3	Forest and grassland	75.02
4	Water body	2.20

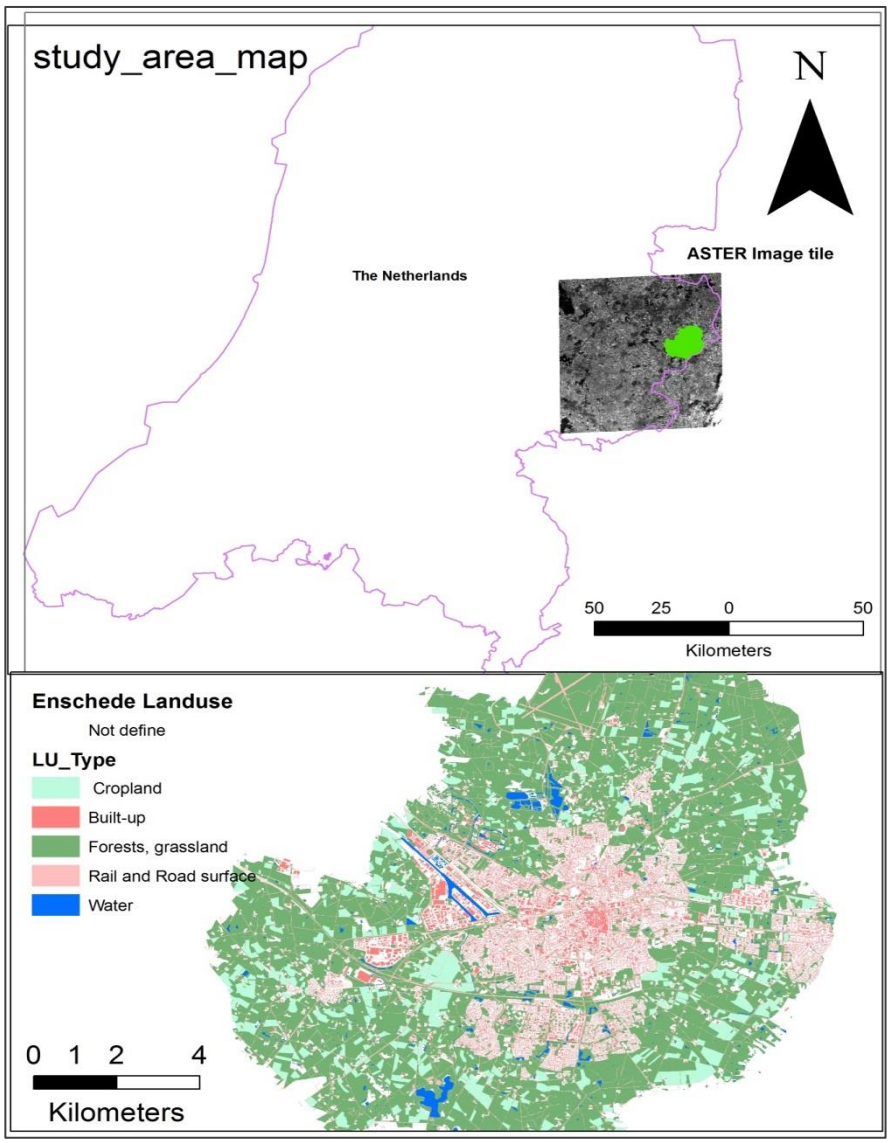

Figure 2.1 The study area (Enschede Municipality) with an ASTER image (as background) and Landuse map with 5 major classes.

The presented Land Use map is in raster form with 15 m resolution, converted from the vector form.

Another Landuse map was created from "Built-up" and "rail and road surface" classes where detail built-up subclasses were used and this land use map is named as Built-up class map.

The Built-up class has the area of 8.44 km², and classified into 16 sub- classes such way that it mostly preserves the original building classification that found in the input data, Top10VectorNL. Adding *rail and road surface* class into built-up sub-class in total 17 types built-up class considered for this study as shown in Table 2.4 and Figure 2.2.

The provided data (Top10VectorNL) was not included building height information which was also required to calculate surface roughness. A 3-D version of topographic might include building height information. However, due to lack of data availability, surface roughness parameter is excluded from the analysis which was mentioned in the objective at proposal phase of thesis.

Table 2.4 the list of 17 Built-up sub-classes with area (m²)

Sl no	Zonecode	Original classes (Type Gebow)	New sub-class (Build-up)	Area (m²)
1	2	Gemeentehuis	Cityhall	3,099.58
2	13	Treinstation	Train-station	3,395.64
3	9	Politiebureau	Police-station	8,089.22
4	12	Sporthal, zwembad	Sport-hall	9,992.94
5	0	Cematorium, tank, toren, watertoren, windmolen	others(cem., tank, toren etc)	12,843.32
6	10	Postkantoor	Post-office	14,064.67
7	6	Manege	Riding school	15,739.11
8	8	Parkeerdak, parkeerdek, parkeergarage	Parkings	23,972.28
9	11	Religieus gebouw	Religious building	29,411.93
10	4	Kas, warenhuis	Departmental shops	35,805.31
11	14	Universiteit	University	40,080.71
12	15	Overig (hoogbouw)	Residential high-rise	51,677.80
13	5	Kliniek, inrichting, sanatorium, ziekenhuis, Psychiatrisch ziekenhuis, psychiatrisch centrum	Hospital and clinic	67,673.33
14	1	Fabriek	Factory	1,99,874.07
15	3	Huizenblok	Houseblock (commercial)	2,34,357.45
16	7	Overig (laagbouw)	Residential low-rise	7,693,702.01
17	16	Rail and Road surface	Rail and Road surface	11,145,308.57

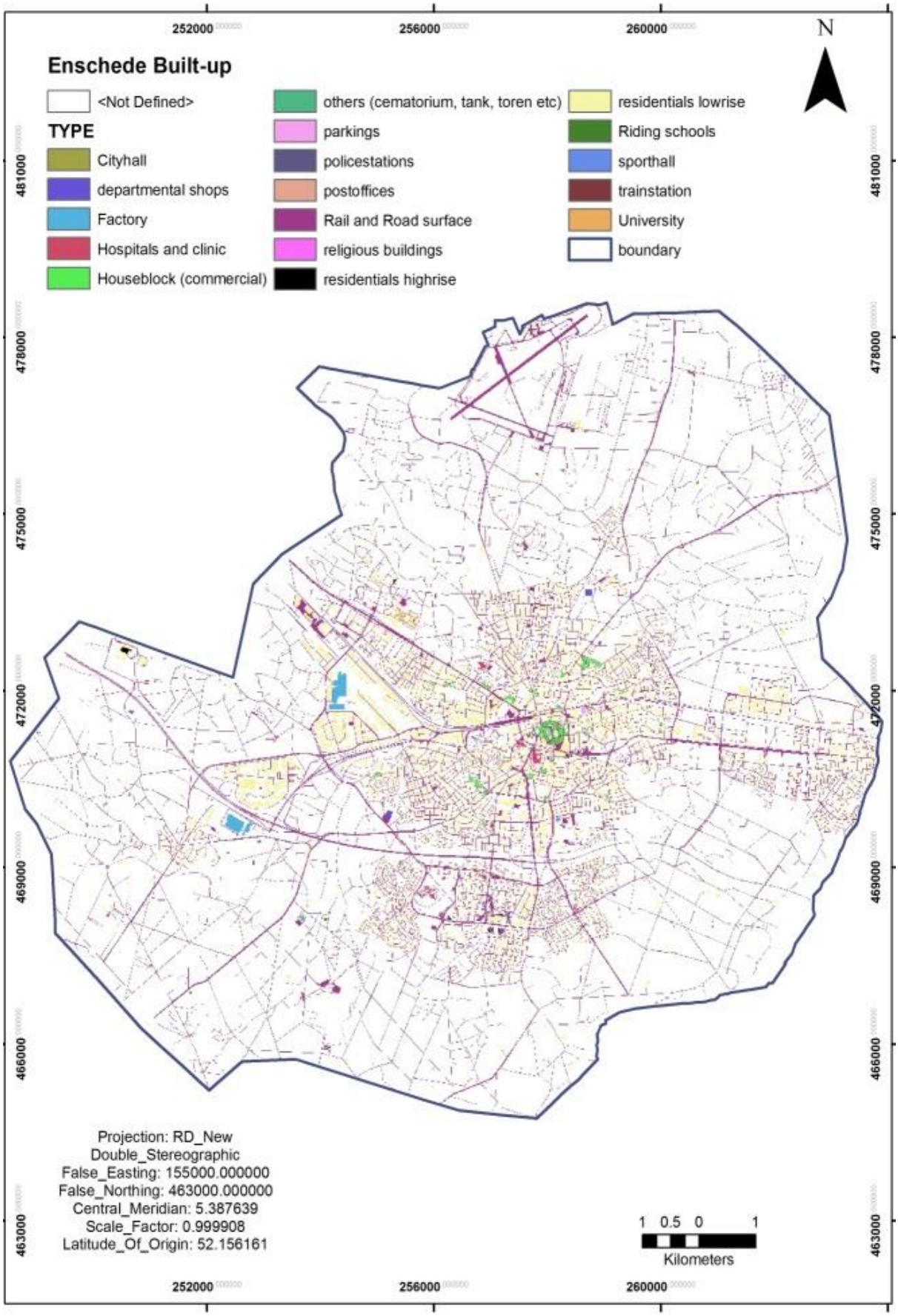

Figure 2.2 Enschede Built-up area map in raster form with 15m resolution

2.4. ASTER Image Pre-processing

Raw image provided in HDF data format which was imported to ILWIS. The preprocessing and derivation of LST and other variables were done using this software.

At-sensor radiances measured in wavelength region is converted to Digital Numbers (DNs). DN values are converted to radiance, then to at-sensor (top-of-atmosphere) reflectance/ brightness temperature and, further, to surface reflectance through atmospheric correction and LST using retrieval algorithm. The steps of calculation of top-of-the-atmosphere (TOA) reflectance at sensor, surface reflectance and brightness temperature (radiometric temperature), true kinetic temperature (land surface temperature, LST) from Digital number (DN) of ASTER Level 1B version 2.13 data are describes below with results.

2.4.1. Calculating spectral reflectance

2.4.1.1. DN to spectral radiance

ASTER L1B data are L1A data with radiometric and geometric coefficients applied (Abrams, 2001). All of these data are stored within metadata in one HDF file. The L1B image is projected onto a rotated map (rotated to "path oriented" coordinate) at full instrument resolutions. ASTER L1B data (after radiometrically re-calibrated) has the form of digital numbers, 8bit (1-255) for visible and near-infrared bands and 12bit (1-4095) for thermal infrared (TIR) bands.

$$L_{rad,j} = (DN_j - 1) \times UCC_j \text{ ---------- (eq. 2.1)}$$

Where, $L_{rad,j}$ = ASTER spectral radiance at the sensor's aperture measured in a wavelength j; j = the ASTER band number; DN_j = Unitless DN values for an individual band j; UCC_j = the Unit Conversion Coefficient ($W\ m^{-2}\ sr^{-1}\ \mu m^{-1}$) obtained from ASTER user guide for each band. There is no difference between converting DNs to radiance of thermal or optical data. The HDF format data has been imported to specific ASTER format in ILWIS software environment. The following equations have been applied to obtain radiance from DN. High gain (UCC) for band 1-2 and normal gain (UCC) for band 3-9 for ASTER L1B metadata sense date 31/05/2003 (appendix-A). The histogram shows (in Appendix-B) radiance value for VNIR_1, SWIR_4 and TIR_10 band. The converted radiance has the geophysical unit of radiance W m^{-2} sr^{-1} μm^{-1} .The output value has the range of 0-250 for VNIR and SWIR and 0-20 for TIR band.

2.4.1.2. TOA reflectance to surface reflectance

Surface reflectance is calculated from TOA reflectance using ILWIS operation "SMAC" in order to provide atmospherically corrected data. The atmospheric corrections are required to satellite data because; various scattering and absorption effects affect Radiance measured by the sensor at the top of the atmosphere. Air molecules (Rayleigh scattering), aerosols (Mie scattering), water vapor and ozone, and the ionosphere (though the ionosphere has little effect on visible and infrared radiation) scatter or absorb signals before receiving by the sensor. The above effects on radiation can be estimate by applying model, which considers radiative transfer equations given inputs such as atmospheric profiles of pressure, temperature and humidity at the time of measurement. Fig. 2.3 shows a SMAC window of ILWIS to do atmospheric correction for each band. The optical thickness and water vapor content values are collected from NASA-AERONET site at the time when the satellite was acquired. Other inputs are also collected from metadata (angles), weather station (pressure) and documentations listed in Table 2.5.

Water vapor content in the atmosphere is a very significant for term in the correction of optical remote sensing data. Nowadays, the common atmospheric correction models use a single value of the average water vapor content of the study area to perform atmospheric correction. As the distribution of water vapor content varies with time and space, it could not be fully accurate to represent the total water vapour

conditions of the whole area by just reading the average value of water vapor content. Yin Zhang, Wang, & Chen (2012) implemented an improved atmospheric correction 6S code by using water vapor content distribution map from MODIS data. They found that the pixel value range of the image is extended. However, the mean pixel value difference of the two corrected images (with water vapor map and with average water vapor value) is not very high (0.028909).

In this study all inputs are in average value over the study area rather using maps. Since the main focus of this study is related to LST obtained from thermal bands, simplified processes of atmospheric correction (without using maps of supporting data) to optical band may not affect the aim of this study. However, Figure 2.4 shows the effect of corrections from a plot between before and after applied the tool on VNIR band1. Value attenuated at lower reflectance and increased at higher Reflectance. The correction was applied on all (9) optical bands.

Table 2.5 List of supporting data to apply atmospheric correction on optical bands

Descriptions	Image day	Source/Remarks
Acquisition Date	2003-05-31	ASTER Image metadata
Julian day	151	http://landweb.nascom.nasa.gov/browse/calendar.html
Time of Day	10:45:22 UTC	metadata
Local time	12:45 CEST	http://www.timezoneconverter.com/cgi-bin/tzc.tzc
Optical Thickness at 550 nm . Smac allowed range: 0.05 to 0.8.	0.388	AERONET (AErosol RObotic NETwork) by NASA: http://aeronet.gsfc.nasa.gov/
Water Vapour (gmcm-2)	0.647	AERONET (AErosol RObotic NETwork) by NASA: http://aeronet.gsfc.nasa.gov/
Ozone (atm.cm)	0.33	http://ozonewatch.gsfc.nasa.gov/facts/dobson.html
Surface pressure (hPa)	1012.4	Hourly KNMI observation at station Twente : Pressure relative to sea level during the observation
Solar Zenith angle (90-SEA) in deg	31.48	ASTER Image metadata
Solar Azim Angle in deg	159.5339	ASTER Image metadata
Sensor Zenith angle	0	
Sensor Azimuth angle	0	
Air temperature (degrees Celsius)	25.2	Hourly KNMI observation at station Twente http://www.knmi.nl/klimatologie/uurgegevens/select_uur.cgi?language=nl , Temperature at 1.50 m height during the observation
Cloud cover Invisible (9) to visible(0)	0	Hourly KNMI observation at station Twente :Cloud cover (canopy cover of the upper air into eighths), during the observation (9 = upper air invisible)
wind speed (m / s)	3	Hourly KNMI observation at station Twente : Hourly average wind speed

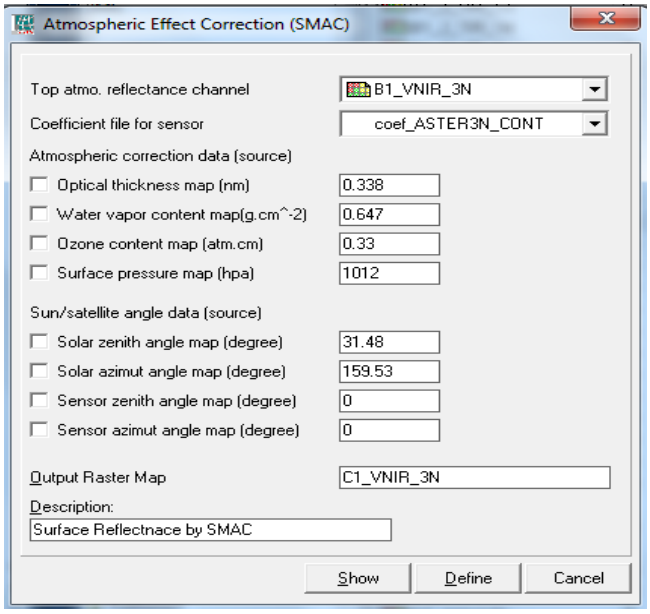

Figure 2.3 A SMAC window of ILWIS software filled all inputs corresponding to input TOA reflectance of VNIR_1 band for an image acquired at 31th may, 2003

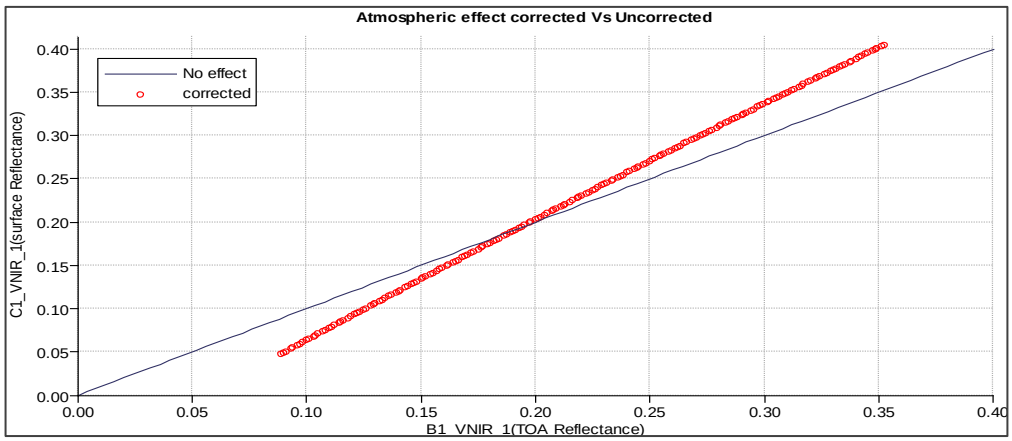

Figure 2.4 Effect of atmospheric correction on VNIR band 1

Corrected surface reflectance bands are used to derive NDVI, NDBI, Albedo and Emissivity.

2.4.2. Processing of thermal bands

2.4.2.1. TIR re-calibration due to temporal decline

The conversions of DNs to radiance for thermal bands are same as optical band as discussed earlier. However, additional calibration of thermal data is required due to temporal decline of detectors responsively as suggested by JPL-NASA. The re-calibration aimed to correct for temporal decline of the detectors responsively between consecutive changes in the radiometric calibration coefficient (RCC) has been applied for RCC versions of 3.x or higher. ASTER TIR products with RCC versions 1.x and 2.x (2.17, 2.18 and 2.20, respectively) need to be re-calibrated for this matter using the linear function below

$$L_{rad,j}(c) = A_j \times L_{rad,j} + B_j \text{ ---------- (eq.2. 2)}$$

Where, $L_{rad,j}$ (c) refers to the re-calibrated spectral radiance, A and B are re-calibration coefficients for a band j found http://tonolab.cis.ibaraki.ac.jp/ASTER/RECAL/.

Table 2.6 Results of re-calibration of TIR data due to temporal decline

TIR Band	Before		After	
	Min Radiance	Max Radiance	Min Radiance	Max Radiance
10	6.221	11.3722	6.229	11.409
11	6.766	12.366	6.791	12.418
12	7.117	12.613	7.133	12.681
13	7.463	12.547	7.548	12.591
14	7.309	11.578	7.346	11.618

2.4.2.2. Spectral radiance to TOA brightness temperature

The brightness temperature was calculated by applying ILWIS SEBS tool for TIR 13 and 14 based on Plank's radiation function. Theories are also documented in ILWIS help system. This temperature is used in LST derivation.

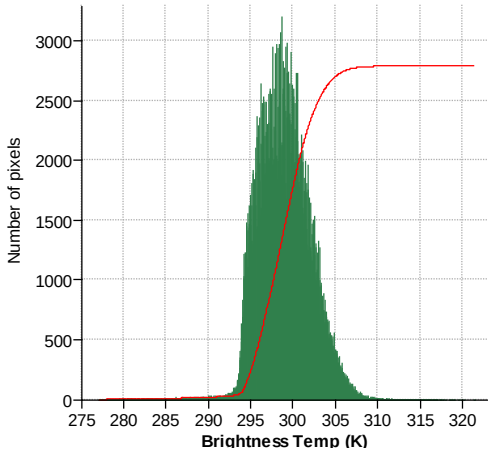

Figure 2.5 Histogram of brightness temperature at TIR band 13 (Min: 277, Max 321, Avg: 297K)

2.5. Image Processing

2.5.1. Derivation of Broadband Surface Albedo

The VNIR and SWIR bands of ASTER provide surface reflectance. These narrow bands reflectance can be combined into the broad band reflectance to obtain surface albedo. Remote sensing instruments do not directly measure surface albedo. As a result, albedo must be inferred through a series of manipulations to the raw remote sensing data, starting with selecting cloud-free pixels within the data. These raw data are originally stored as digital numbers need to calibrate in order to represent geophysical unit of radiance ($Wm^{-1}sr^{-1}$). The radiance at the top of the atmosphere (TOA) needs to be corrected for the effects of the intervening atmosphere. The data can then be divided by the Planck irradiance curve to derive the surface reflectance. The albedo is an integration of reflectance over all view angles, but satellite instruments only take measurements at one or a few viewing angles. Therefore, a computation needs to perform to estimate albedo from reflectance, which requires an understanding of the BRDF of the surface being measured. However, the calculation of BRDF can be ignored assuming the surface as Lambertian. Atmospheric correction produces surface spectral reflectance. If the surface is a Lambertian, spectral reflectance is equal to spectral albedo. This simplification can lead to larger error from +/- 0.02 (base error) to +/- 0.05, which is still acceptable for the application of albedo in GCMs (Maurer, 2002). Lastly, albedo retrieved from separate narrowband channels need to be converted into broadband region of solar radiation of approximately 0.3-3.0 micrometer.

Table 2.7 The following Table will represent the necessary steps that need to be performed to the raw remote sensing signal in order to convert them into broadband albedo at the surface

Input	Step/processes	Output
Pixels (Digital number-DN)	Cloud-mask	Cloud-free pixels (DN)
DN	Calibration (find accurate and up-to-date coefficients for used instrument)	Radiance ($Wm^{-2}sr^{-1}$)
Radiance (TOA)	Atmospheric corrections	Reflectance (surface)
Reflectance	Anisotropic correction or, Lambertian spectral	Albedo (narrowband)
Narrowband albedo	Narrowband-To-Broadband (NTB) conversion	Broadband albedo

Narrow-to-broadband albedo:
Although, ASTER has the largest number of narrow bands in the visible and near-IR spectrum (9 bands), most bands are in the near-IR region and apparently are not the best for distinguishing different surface reflectance spectra (Liang, 2000).The nine NVIR and SWIR channels allow to effectively converting narrowband to broadband albedos. The linear conversion formula proposed by Liang (2000):

$$\alpha_{short} = 0.484\alpha_1 + 0.335\alpha_3 - 0.324\alpha_5 + 0.551\alpha_6 + 0.305\alpha_8 - 0.367\alpha_9 - 0.0015$$ --(eq. 2.3)

Here, α_{short} is the shortwave broadband albedo. And $\alpha_i (i = 1\ to\ 9)$ are the spectral albedos of the respective channels.

It is evident that not all of bands are necessary to calculate broadband albedos. For example, only six bands are needed to calculate the total shortwave albedo. For visible broadband albedos, the coefficients of eight bands are provided. Chrysoulakis (2003) used shortwave broadband albedo (α_{short}) to estimate all-wave urban surface radiation balance. Hence, in the context of this study, consideration of α_{short} would be enough to create albedo map in the study area.

The Eq (2.3) were scripted and applied in ILWIS to derive the broadband surface albedo. The output map was in 30 m resolution, since SWIR band were related to the calculation.

2.5.2. Derivation of NDVI

The normalized difference vegetation index (NDVI) can be obtained using ration calculation between the near infrared (NIR) band and the red (R) band using the equation

$$NDVI = \frac{\rho_{NIR} - \rho_R}{\rho_{NIR} + \rho_R}$$ ---------- (eq 2.4)

Where, ρ_{NIR} and ρ_R are atmospherically corrected surface reflectance in the near infrared and red bands respectively.

The output map was in 15 m resolution.

2.5.3. Derivation of NDBI

The normalized difference build-up index is used to strengthen building information and extract the build-up land from urban areas (Liu & Zhang, 2011). The NDBI is the reflectivity of urban building and is higher in the fifth band than the forth band, can be calculated as follows

$$NDBI = \frac{\rho_{MIR}-\rho_{NIR}}{\rho_{MIR}+\rho_{NIR}} \text{ ---------- (eq 2.5)}$$

The output map was in 30 m resolution.

2.5.4. Derivation Land surface emissivity

The emissivity largely depends on the surface roughness and nature of surface cover. Due to the unavailability of building height data in the study area emissivity derivation was done using built-in ILWIS tools, where the algorithm use NDVI and vegetation surface roughness height. The surface emissivity was calculated using band 2, 3N and surface albedo map as input. The output image was in 30m resolution.

2.5.5. Retrieval of LST

Split window algorithm has been proposed by Qin *et al.,* (2006) to retrieve LST (RMSD= 0.9K) from ASTER thermal bands (13, 14). A more accurate algorithm, Temperature-Emissivity Separation (TES) to retrieve LST (RMSD=0.3k) requires *in situ* parameters of atmospheric profiles simultaneously to the satellite overpass. Since in urban heat island studies, we are focusing on land surface temperature and human thermal comfort zone changes from favourable to non-favourable gradually (Fig. 2.6), LST retrieved using split window algorithm (with 1k error) may not influence LST significantly.

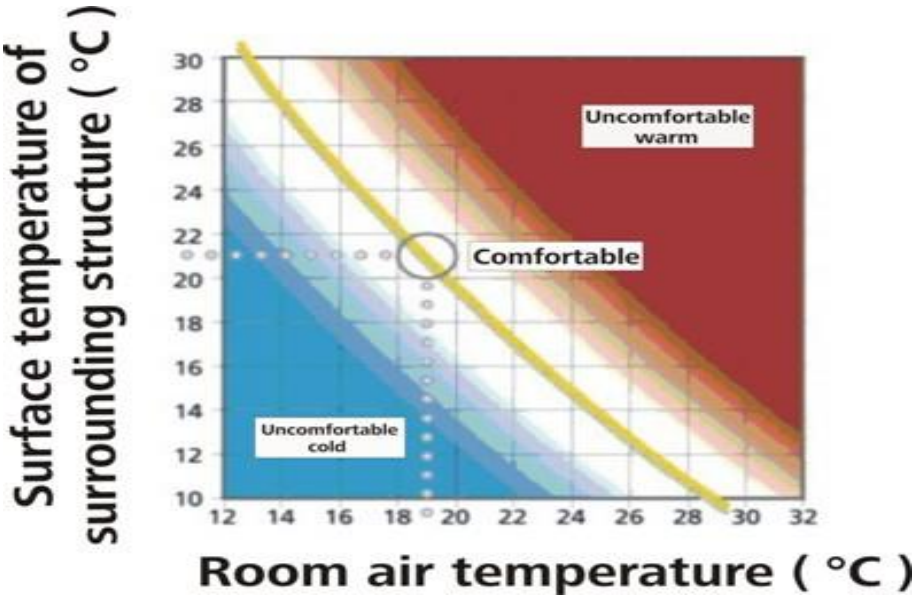

Figure 2.6 human thermal comfort level from comfortable to uncomfortable zone changes gradually. Image source: (Cohen, Potchter, & Matzarakis, 2013).

Figure 2.6 shows surface temperature is slightly higher than air temperature. Therefore, land surface temperature retrieved from an algorithm with the accuracy around 1k would be sufficient for this study.

The flow chart (in Figure 2.7) shows the LST retrieval processes and obtaining surface albedo and emissivity from ASTER level 1B product. To retrieve LST from ASTER images by split window algorithm three parameters are required: Brightness Temperature of Band 13 and 14, water vapor content and the third parameter is emissivity. ILWIS SEBS tool contains this algorithm. The output was in 90 m resolution.

Derived all images then imported to AcrGIS with proper projections transformation and selected area that covers the Enschede Municipality. In total 5 satellite-image derived maps and 2 raster landuse maps were

ready of perform analysis and test hypothesis. The analysis was performed in ArcGIS, IDRISI, R and M.S. Excel. Detail flowcharts (in GIS model-builder) of the analysis are attached in Appendix-D.

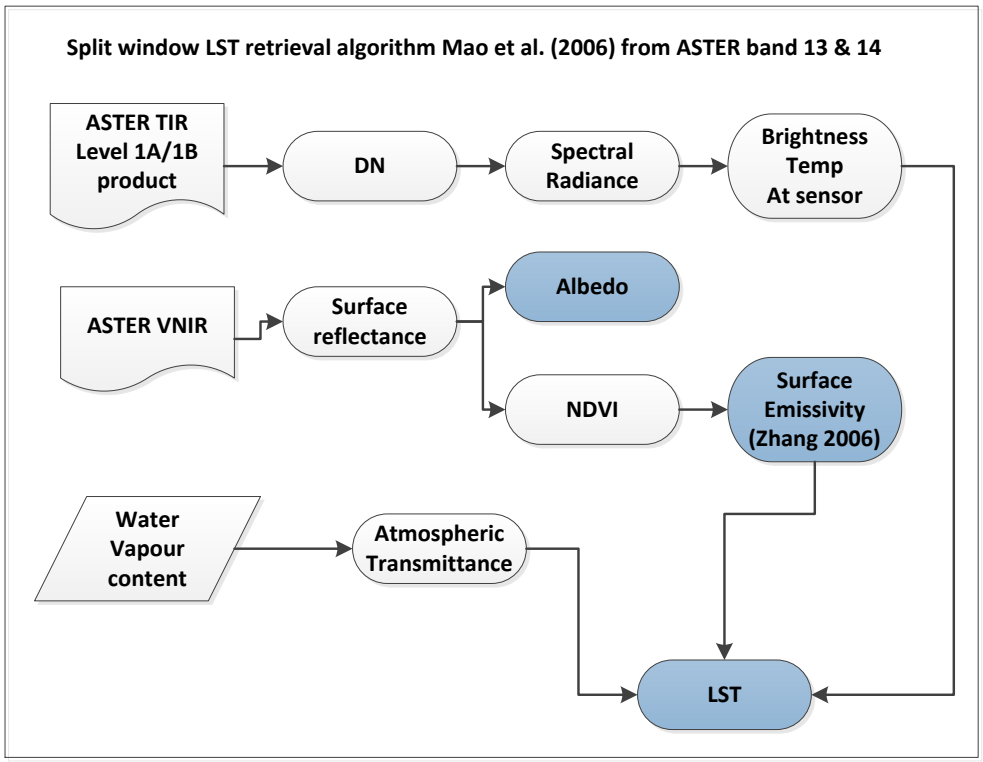

Figure 2.7 Methodology Flowchart for LST retrieval algorithm

2.6. Assumptions for Hypothesis test

2.6.1. To Test the Distribution of LST and Emissivity in Built-up area

The Kruskal–Wallis H (Kruskal & Wallis, 1952) test is used when data have one nominal variable and one ranked variable. It tests whether the mean ranks are the same in all the groups i.e., if there are statistically significant differences between two or more groups of an independent variable (built-up classes) on a continuous or ordinal dependent (LST) variable. When measurement variable does not meet the normality assumption of a one-way ANOVA, a non-parametric Kruskal–Wallis test is suitable (McDonald, 2014).

Assumptions:

- Dependent variable should be ordinal or continuous (i.e., interval or ratio)
- Independent variable should be two or more categorical, independent groups.
- Observations (samples) should be independent (no relationship between samples in each group)
- Distributions for each group of the independent variable have the same shape (also with same variability). If the distributions have the same shape test will compare the medians of dependent variable (LST). If the distributions have a different shape test will compare mean ranks.

The Kruskal–Wallis Test cannot tell which specific groups of independent variable are statistically significantly different from each other; it only tells that at least two groups were different. To determine which of these groups differ from each other, can test using a post hoc test.

2.6.2. Regression Model Hypothesis Test

The assumptions for multiple regression explained by Rossiter (2012); Adam & Lund (2013); Chatterjee & S. (2012) are

(1) Dependent variable should be measured on a continuous scale,
(2) At least two independent variables which can be continuous or categorical,
(3) A linear relationship between dependent variable and each independent variables,
(4) The response is some deterministic linear function of the predictor
(5) Multicollinearity must not exists among independent variables,
(6) There should be no significant outliers, high leverage points or highly influential points and
(7) The residuals should be normally distributed. Typically, assess these assumptions using regression diagnostics.

3. RESULTS AND DISCUSSIONS

3.1. Visual Interpretation of LST and surface parameters imagery

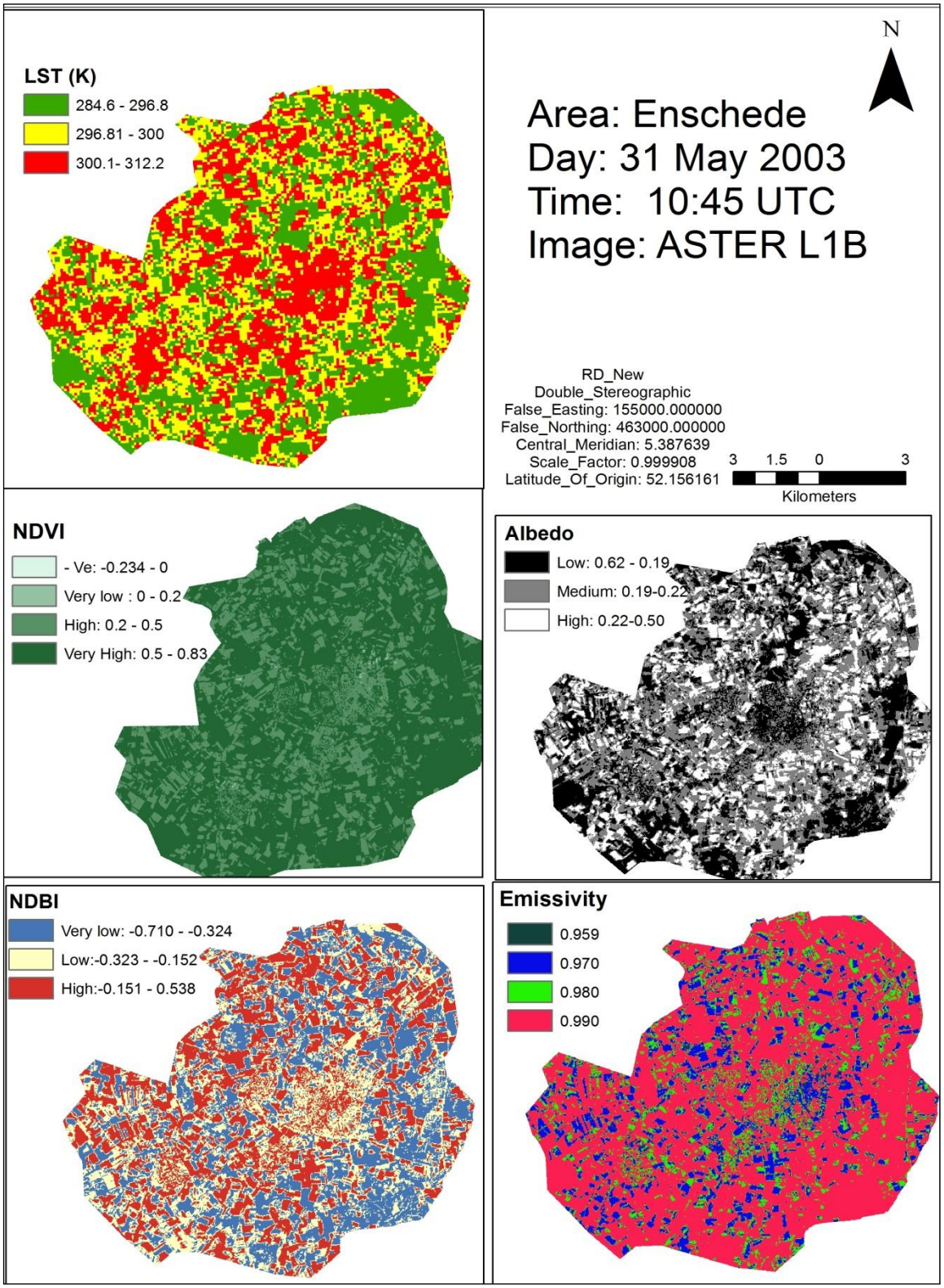

Figure 3.1 Distributions of LST, NDVI, NDBI, Albedo and Emissivity in the study area, computed from a ASTER image

The spatial distribution of LST, NDVI, NDBI, Albedo and Emissivity within the study area is shown in Figure 3.1. The NDVI score is originally in 15 m pixel While, NDBI (30 m resampled to 15m), Albedo (30 m resampled to 15m), Emissivity (30 m resampled to 15m) and LST (90 m resampled to 15m) are actually may not represent the real value if it varies less than its pixel size. Hence any small spatial changes will remain unknown. In general, visual patterns of LST is appears as opposite (high/low) from NDVI, albedo and emissivity. On the other hand, NDBI (built-up indices) shows the similar patterns of LST. For example, a high value range LST cluster (red colour in LST map) concentrated at near the center of the area, also shows higher NDBI and lower albedo, emissivity and NDVI score for that cluster. This map gives an overview on distribution of data and their association. Primary investigation indicates their association clams harmony with theory, at least in the Built-up area. However, the study objected is more specific to the distribution of those variable on built-up detail. The statistical summary will be the next analysis.

3.2. Zonal Statistics of LST, NDVI, NDBI, Albedo and Emissivity

The *zonal statistics* in Arcgis has been applied to the NDVI (15 m), NDBI (30 m resampled to 15m), Albedo (30 m resampled to 15m), Emissivity (30 m resampled to 15m) and LST (90 m resampled to 15m) with 15m raster landuse and Built-up map separately analysed values per class.

Zonal Statistics is calculated for each zone defined by a zone dataset, based on values from another dataset (a value raster). A single output value is computed for every zone (per class) in the input zone dataset. Results are shown in Table 3.1 to 3.5 as MEAN (the average of the values in each zone is assigned to all output cells in that zone), MEDIAN (the median value in each zone is assigned to all output cells in that zone), minimum, maximum, standard deviation for the built-up classes to LST, Emissivity, Albedo, NDBI and NDVI , respectively. Each table is arranged by median value (highlighted) for all parameters. Similar statistics table for Landuse class has also attached in the Appendix –C and found Built-up and rail and road surface landuse classes appeared as warmer than vegetation landcover. Higher median LST observed (Table 3.1) in the policestation (302.6K), parking (302.1K), and hospital area (302.1K) than Factory (300.1K), high-rise residential (300.5K), road surface (298.9K). This (in Table 3.1) order of LST across built-up area did not match with the preliminary order mentioned in the research hypothesis.

Table 3.1 Zonal Statistics of LST for Enschede Built-up area

TYPE/LST	ZONE_CO	AREA	MIN	MAX	RANGE	MEAN	STD	MAJORITY	MINORITY	MEDIAN
policestations	10	8550	294.8	303.3	8.5	300.9	3.0	302.6	295.2	302.6
parkings	9	24300	294.6	304.1	9.5	301.6	2.4	302.0	300.6	302.1
Hospitals and clinic	6	66375	291.1	304.9	13.8	300.8	2.9	302.8	293.8	302.1
Houseblock (commercial)	4	232200	293.0	306.8	13.8	301.4	2.1	302.5	293.0	301.7
sporthall	13	10125	292.7	303.3	10.6	300.2	2.8	302.2	299.0	300.8
residentials highrise	16	50625	294.4	306.4	12.0	299.4	3.3	301.8	294.4	300.5
Cityhall	3	2250	300.4	302.0	1.6	300.9	0.7	300.4	302.0	300.4
trainstation	14	3825	300.1	300.4	0.3	300.2	0.1	300.1	300.4	300.1
Factory	2	198225	287.3	308.7	21.4	299.5	3.1	300.6	302.7	300.1
postoffices	11	15300	294.8	303.6	8.8	300.4	2.6	303.6	295.3	300.0
religious buildings	12	28125	292.7	305.2	12.5	299.2	3.2	302.1	294.3	299.6
residentials lowrise	8	7706030	285.4	312.2	26.8	299.3	3.3	295.1	287.1	299.4
others (cematorium, tank, toren etc)	1	13725	288.3	305.4	17.1	298.7	2.5	299.3	288.3	299.3
Rail and Road surface	17	11137300	284.6	312.2	27.6	299.0	3.3	295.1	284.8	298.9
departmental shops	5	36000	292.0	305.5	13.5	298.9	2.2	298.7	292.0	298.7
University	15	39150	295.8	308.5	12.7	298.9	2.9	300.1	298.0	298.6
Riding schools	7	15525	290.3	306.4	16.1	298.3	3.6	300.6	290.3	298.5

Table 3.2 Zonal statistics of Emissivity for Enschede Built-up area

TYPE/Emissivity	ZONE_CO	AREA	MIN	MAX	RANGE	MEAN	STD	MAJORITY	MINORITY	MEDIAN
Cityhall	3	2250	0.970	0.980	0.010	0.975	0.005	0.970	0.970	0.970
trainstation	14	3825	0.959	0.990	0.031	0.979	0.007	0.980	0.959	0.980
parkings	9	24300	0.970	0.990	0.020	0.981	0.008	0.990	0.970	0.980
Houseblock (commercial)	4	232200	0.959	0.990	0.031	0.982	0.008	0.990	0.959	0.980
residentials highrise	16	50625	0.970	0.990	0.020	0.982	0.008	0.990	0.970	0.980
sporthall	13	10125	0.970	0.990	0.020	0.983	0.007	0.990	0.970	0.980
policestations	10	8550	0.970	0.990	0.020	0.984	0.007	0.990	0.970	0.980
University	15	39150	0.970	0.990	0.020	0.983	0.009	0.990	0.980	0.990
Hospitals and clinic	6	66375	0.970	0.990	0.020	0.984	0.008	0.990	0.970	0.990
Factory	2	198225	0.959	0.990	0.031	0.984	0.009	0.990	0.959	0.990
residentials lowrise	8	7706030	0.959	0.990	0.031	0.985	0.008	0.990	0.959	0.990
Rail and Road surface	17	11137300	0.959	0.990	0.031	0.985	0.008	0.990	0.959	0.990
religious buildings	12	28125	0.970	0.990	0.020	0.986	0.006	0.990	0.970	0.990
Riding schools	7	15525	0.970	0.990	0.020	0.987	0.005	0.990	0.970	0.990
departmental shops	5	36000	0.970	0.990	0.020	0.987	0.006	0.990	0.970	0.990
others (cematorium, tank, toren etc)	1	13725	0.970	0.990	0.020	0.987	0.006	0.990	0.970	0.990
postoffices	11	15300	0.970	0.990	0.020	0.988	0.004	0.990	0.970	0.990

Table 3.3 Zonal statistics of Albedo for Enschede Built-up area

TYPE/Albedo	ZONE_CODE	AREA	MIN	MAX	RANGE	MEAN	STD	MAJORITY	MINORITY	MEDIAN
Cityhall	3	2250	0.167	0.188	0.021	0.178	0.007	0.170	0.167	0.177
Trainstation	14	3825	0.167	0.190	0.023	0.181	0.007	0.184	0.185	0.184
Parkings	9	24300	0.152	0.203	0.051	0.188	0.010	0.184	0.152	0.188
Houseblock (commercia	4	232200	0.153	0.285	0.132	0.195	0.018	0.189	0.220	0.192
Hospitals and clinic	6	66375	0.165	0.265	0.100	0.201	0.022	0.181	0.208	0.194
University	15	39150	0.148	0.289	0.141	0.205	0.028	0.189	0.177	0.194
Postoffices	11	15300	0.175	0.242	0.067	0.199	0.015	0.183	0.175	0.196
Religious buildings	12	28125	0.164	0.270	0.106	0.202	0.021	0.192	0.164	0.196
Policestations	10	8550	0.177	0.225	0.048	0.201	0.012	0.210	0.178	0.202
Residentials lowrise	8	7706030	0.086	0.424	0.338	0.206	0.027	0.194	0.094	0.202
Departmental shops	5	36000	0.143	0.268	0.125	0.200	0.022	0.195	0.183	0.203
Rail and Road surface	17	11137300	0.093	0.469	0.376	0.207	0.029	0.191	0.093	0.204
Factory	2	198225	0.149	0.457	0.308	0.212	0.036	0.213	0.159	0.206
Riding schools	7	15525	0.169	0.278	0.109	0.210	0.022	0.224	0.179	0.207
Residentials highrise	16	50625	0.125	0.261	0.136	0.213	0.029	0.202	0.125	0.208
sporthall	13	10125	0.185	0.239	0.054	0.208	0.015	0.205	0.185	0.209
Others (cematorium, tai	1	13725	0.158	0.259	0.101	0.214	0.019	0.225	0.158	0.217

Table 3.4 Zonal statistics of NDBI for Enschede Built-up area

TYPE/NDBI	ZONE_CODE	AREA	MIN	MAX	RANGE	MEAN	STD	MAJORITY	MINORITY	MEDIAN
sporthall	13	10125	-0.414	-0.012	0.402	-0.185	0.160	-0.042	-0.261	-0.082
residentials highrise	16	50625	-0.439	0.049	0.488	-0.164	0.149	-0.019	-0.439	-0.127
policestations	10	8550	-0.402	-0.025	0.377	-0.161	0.103	-0.121	-0.192	-0.138
Cityhall	3	2250	-0.183	-0.070	0.113	-0.136	0.040	-0.183	-0.140	-0.140
parkings	9	24300	-0.471	-0.052	0.419	-0.169	0.089	-0.125	-0.471	-0.153
Houseblock (commercial	4	232200	-0.429	0.019	0.448	-0.165	0.078	-0.104	-0.418	-0.156
trainstation	14	3825	-0.268	-0.112	0.156	-0.164	0.046	-0.129	-0.139	-0.169
Hospitals and clinic	6	66375	-0.399	0.011	0.410	-0.178	0.099	-0.132	-0.395	-0.172
Factory	2	198225	-0.439	0.065	0.504	-0.209	0.118	-0.130	-0.392	-0.205
residentials lowrise	8	7706030	-0.549	0.129	0.678	-0.219	0.134	-0.134	-0.549	-0.216
Rail and Road surface	17	11137300	-0.562	0.168	0.730	-0.221	0.141	-0.326	-0.562	-0.229
departmental shops	5	36000	-0.422	0.025	0.447	-0.248	0.126	-0.421	-0.407	-0.236
religious buildings	12	28125	-0.475	-0.012	0.463	-0.240	0.118	-0.296	-0.475	-0.245
University	15	39150	-0.429	0.127	0.556	-0.202	0.157	-0.412	-0.422	-0.248
Riding schools	7	15525	-0.434	-0.018	0.416	-0.240	0.111	-0.158	-0.434	-0.251
postoffices	11	15300	-0.426	-0.058	0.368	-0.260	0.101	-0.384	-0.408	-0.279
others (cematorium, tanl	1	13725	-0.438	0.046	0.484	-0.278	0.122	-0.376	-0.438	-0.335

Table 3.5 Zonal statistics of NDVI for Enschede Built-up area

TYPE/NDVI	ZONE_CODE	AREA	MIN	MAX	RANGE	MEAN	STD	MAJORITY	MINORITY	MEDIAN
Cityhall	3	2250	0.329	0.587	0.258	0.453	0.078	0.329	0.329	0.449
trainstation	14	3825	0.376	0.654	0.278	0.467	0.068	0.413	0.376	0.454
parkings	9	24300	0.179	0.748	0.569	0.458	0.112	0.322	0.179	0.460
policestations	10	8550	0.322	0.730	0.408	0.495	0.115	0.397	0.322	0.483
Houseblock (commercial)	4	232200	0.185	0.758	0.573	0.494	0.107	0.449	0.185	0.486
sporthall	13	10125	0.382	0.744	0.362	0.554	0.142	0.390	0.382	0.518
Hospitals and clinic	6	66375	0.202	0.746	0.544	0.533	0.118	0.464	0.202	0.520
residentials highrise	16	50625	0.259	0.805	0.546	0.544	0.140	0.708	0.259	0.530
Factory	2	198225	0.025	0.786	0.761	0.555	0.158	0.737	0.025	0.575
residentials lowrise	8	7706030	0.025	0.815	0.790	0.570	0.140	0.726	0.025	0.587
religious buildings	12	28125	0.310	0.757	0.447	0.581	0.120	0.693	0.310	0.591
Riding schools	7	15525	0.296	0.734	0.438	0.586	0.116	0.528	0.296	0.601
Rail and Road surface	17	11137300	-0.019	0.829	0.848	0.580	0.140	0.726	-0.019	0.613
departmental shops	5	36000	0.201	0.752	0.551	0.598	0.117	0.636	0.201	0.636
postoffices	11	15300	0.382	0.740	0.358	0.623	0.110	0.687	0.382	0.682
University	15	39150	0.265	0.789	0.524	0.599	0.186	0.758	0.265	0.710
others (cematorium, tank, toren	1	13725	0.361	0.794	0.433	0.663	0.119	0.693	0.361	0.714

The median LST value of some Built-up sub-classes are same and the medians are arranged in high to low (for LST and NDBI), and opposite (low to high) for Albedo, Emissivity, and NDVI, highlighted in each Table. Initial assessment is they can be grouped by median value. If it is possible then 17 built-up sub-classes can be reclassifying based on median (or mean) value. However, results from other parameters in Table 3.2 to 3.5 do not show the pattern that was appeared in visual interpretations. Additionally, orders of Built-up sub-classes for each parameter are different. That means it's hard to interpret result from summary statistics. The pixel by pixel analysis in each subclass may be useful to understand the distribution of LST and its association with land surface parameters, will discuss in the next section.

3.3. Cross-tabulation analysis

CROSSTAB tool in IDRISI performs a cross-tabulation analysis that compares images containing categorical variables of two types using hard classification method, where all pixels in the maps have complete membership to exactly one category. The cross-tabulation analysis has applied to the NDVI, NDBI, Albedo, Emissivity and LST with detail Built-up map. Equal percent (around 33%) of pixels (as quantile) were allocated to NDBI, Albedo, Emissivity and LST classification, so that output confusion-matrix can be compare at the same scale. Except NDVI, this was classified based on ranges found at literature as shown in Table 3.6.

Table 3.6 The NDVI value range and corresponding landuse type used in Bottyán *et al.*, (2005); Chen *et al.,* (2006)

Sl no	LC	NDVI value (from articles)	In-data NDVI value range	Used class
1	Water	<0	-0.234 – 0.0	Negative
2	Mixed built up and veg	0.0 - 0.5	0.01 - 0.500	Medium
3	Fully vegetated	>0.5	0.501 – 0.834	High

Table 3.7 The percentage of Pixels from cross-tabulation of Built-up sub-classes (columns) against NDVI (rows)

NDVI (By per cent)	Other	Factor	Cityhall	Com hous	kas	Hospi	riding	low resi	parking	police	post	religious	sporthall	tarin	University	High resi	road	Total
Total (Pixel)	**61**	**881**	**10**	**1032**	**160**	**295**	**69**	**34249**	**108**	**38**	**68**	**125**	**45**	**17**	**174**	**225**	**49499**	**87056**
Zone code	0	1	2	3	4	5	6	7	8	9	10	11	12	13	14	15	16	Total (%)
Negative (-0.234-0)	0	0	0	0	0	0	0	0	0	0	0	0	0	0	0	0	0	0
Medium (0 - 0.5)	13	37	70	54	21	44	17	35	68	61	22	26	49	71	36	49	33	34
High (0.5 - 0.834)	87	63	30	46	79	56	83	65	32	39	78	74	51	29	64	51	67	66
Total (%)	100	100	100	100	100	100	100	100	100	100	100	100	100	100	100	100	100	100

Table 3.7 shows cross-tabulation result obtained from 3 NDVI categories; low (-0.234 to 0), medium (0 to 0.5), high (0.5 – 0.834) and 17 built-ups. The percentage of pixels has complete membership to exactly each NDVI category is highlighted. None of a pixel found in low NDVI category. The reported NDVI value for water body is <0, indicates the reliability of image and its processing. Additionally, higher percentage of pixels from different built-up sub-classes found in high NDVI category indicates abundant greenness in those built-up sub-classes. On the other hand, NDBI value ranges from -0.562 to 0.186 in the built-up area, classified into 3 categories (low, Medium and high) shows random distribution of pixels in each sub-class to all three NDBI categories (Table 3.8).

Table 3.8 The percentage of Pixels from cross-tabulation of Built-up sub-classes (columns) against NDBI (rows)

NDBI	Other	Factory	Cityhall	com. Hou	kas	Hospi	riding	low resi	parking	police	post	religious	sporthall	tarin st	Universi	High resi	road	Total
Total (Pixel)	**61**	**881**	**10**	**1032**	**160**	**295**	**69**	**34249**	**108**	**38**	**68**	**125**	**45**	**17**	**174**	**225**	**49499**	**87056**
Zone code	0	1	2	3	4	5	6	7	8	9	10	11	12	13	14	15	16	Total (%)
Low (-0.562- -0.304)	59	24	0	5	38	12	30	32	7	16	44	35	36	0	38	29	35	33
Medium (-0.304 - -0.143)	21	41	40	53	36	49	51	35	45	24	40	36	11	53	25	19	32	33
High (-0.143 - 0.168)	20	35	60	42	26	39	19	33	47	61	16	29	53	47	37	52	33	33
Total (%)	100	100	100	100	100	100	100	100	100	100	100	100	100	100	100	100	100	100

Table 3.9 The percentage of Pixels from cross-tabulation of Built-up sub-classes (columns) against Albedo (rows)

Albedo (percent)	Other	Factory	Cityhall	Com. Hou	kas	Hospi	riding	low resi	parking	police	post	religious	sporthall	tarin st	Universi	High resi	road	Total
Total (Pixel)	**61**	**881**	**10**	**1032**	**160**	**295**	**69**	**34249**	**108**	**38**	**68**	**125**	**45**	**17**	**174**	**225**	**49499**	**87056**
Zone code	0	1	2	3	4	5	6	7	8	9	10	11	12	13	14	15	16	Total (%)
Low (0.086 - 0.192)	15	28	100	51	19	46	26	34	67	24	34	36	24	100	45	26	33	34
Medium(0.192-0.216)	34	36	0	39	66	25	42	34	33	71	46	46	33	0	25	33	33	34
High(0.216 - 0.469)	51	36	0	10	15	28	32	32	0	5	21	18	42	0	30	41	34	33
Total (%)	100	100	100	100	100	100	100	100	100	100	100	100	100	100	100	100	100	100

Table 3.10 The percentage of Pixels from cross-tabulation of Built-up sub-classes (columns) against emissivity (rows)

Emissivity	Other	Factory	Cityhall	com. Hou	kas	Hospi	riding	low resi	parking	police	post	religious	sporthall	tarin St	University	High resi	road	total
Total (pixel)	**61**	**881**	**10**	**1032**	**160**	**295**	**69**	**34249**	**108**	**38**	**68**	**125**	**45**	**17**	**174**	**225**	**49499**	**87056**
Zone code	0	1	2	3	4	5	6	7	8	9	10	11	12	13	14	15	16	total (%)
Low (0.959-970)	8	18	50	23	7	19	4	17	31	11	1	9	13	18	29	26	16	16
Medium (0.980)	10	19	50	34	14	23	20	17	32	39	16	22	40	65	10	26	16	17
High (0.990)	82	63	0	43	79	58	75	66	37	50	82	70	47	18	61	48	69	67
Total (%)	100	100	100	100	100	100	100	100	100	100	100	100	100	100	100	100	100	100

Similar result found for albedo (Table 3.9) and emissivity (Table 3.10). The purpose was to reclassify Enschede Built-up (17sub-classes) area according to behaviour of those land surface parameters. But none of the built-up sub-classes have the full membership of a category of NDVI, NDBI, Emissivity and Albedo. In other words, cross-tabulation analysis of NDBI, Emissivity and Albedo did not identify similar built-up sub-classes in every case with similar extents. Hence, a distinct reclassification of Built-up areas may not be possible based on the analysis.

Table 3.11 The percentage of Pixels from cross-tabulation of Built-up sub-classes (columns) against LST (rows)

LST	Other	Factory	Cityhall	com. Hou	kas	Hospi	riding	low resi	parking	police	post	religic	sporthall	tarin st	University	High resi	road	Total
Total (pixel)	**61**	**881**	**10**	**1032**	**160**	**295**	**69**	**34249**	**108**	**38**	**68**	**125**	**45**	**17**	**174**	**225**	**49499**	**87056**
zone code	0	1	2	3	4	5	6	7	8	9	10	11	12	13	14	15	16	Total (%)
Low (284.6 - 296.7)	25	21	0	7	34	12	35	33	10	16	10	33	11	0	35	36	36	34
Normal (296.7 -300)	61	58	70	22	44	27	45	33	6	24	46	28	42	100	57	14	34	34
High (300 - 312.2)	15	21	30	71	21	61	20	35	84	61	44	39	47	0	8	50	30	32
Total (%)	100	100	100	100	100	100	100	100	100	100	100	100	100	100	100	100	100	100

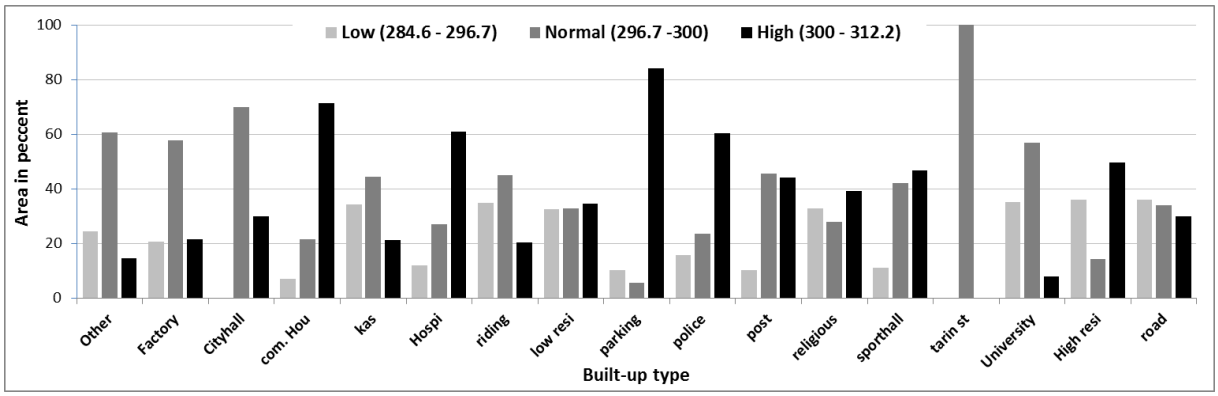

Figure 3.2 The percentage of Pixels in each built-up sub-class corresponding to LST classes

To perform cross-tabulation analysis, LST values have been categorized into 3 equal-pixel classes: low (284.6 to 296.7K), normal (296.7 to 300K) and high (300 to 312.2K). Table 3.11 shows the dominant built-up sub-classes in the high LST class are: commercial (71%), Hospital (61%), parking (84%), police-station (61%), high-rise residential (50%). Obtained result is also plotted in figure 3.2 shows each built-up sub-class (except train-station and cityhall) has the membership of all three thermal classes. Normal LST observed mostly in the factory (58%), cityhall (70%), university (57), train-station (100%) area. Most of the area in cityhall, parking and train-station exhibits as High LST area. On the other hand, LST are almost equally distributed in Road surface and low-rise residential area.

The distribution of LST (observed at 31th may, 2003) in Enschede built-up area is shown as map the Figure 3.3. The LST map shows high value (>300K) of surface temperature is concentrated at the center on the map (commercial area). The surface temperature over that area is higher than the air temperature (298.2K) at the time when LST were estimated. A higher proportion of NDBI and lower albedo in the "commercial area" built-up sub-class (see Table 3.8 & 3.9), would be an explanation for such high surface temperature at that area. This information (finding relationship between LST and NDBI, albedo or with other variables) would be useful for implementation purpose of this study. However, to confirm whether the LST of a class is different from other built-ups, a hypothesis test is still important. The next section is to perform hypothesis tests that are formulated in the research objectives section.

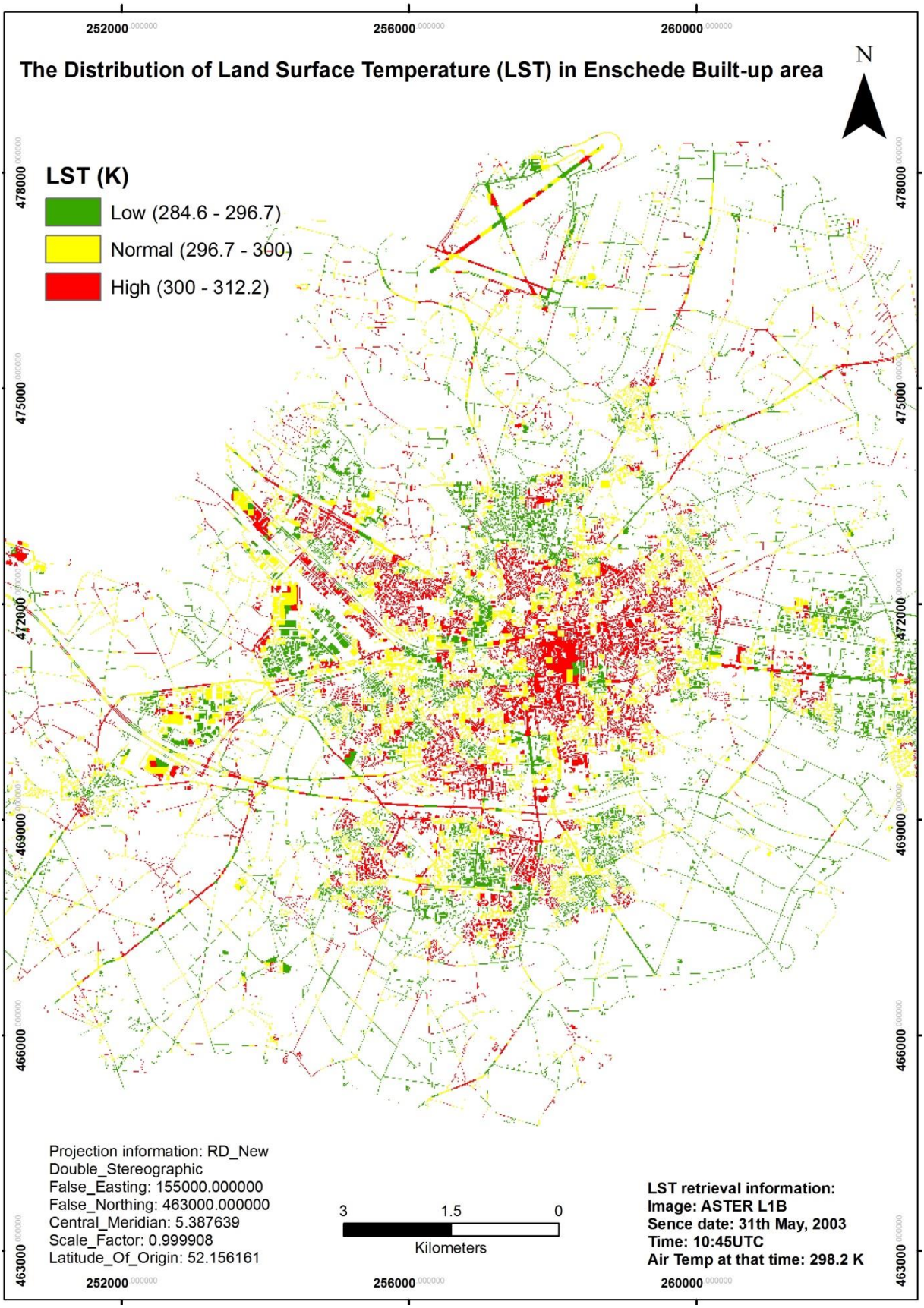

Figure 3.3 The LST distribution in Enschede Built-up area. LST Retrieved from ASTER on 31th may, 2003 at 12.45 PM (local time).

3.4. Hypothesis Tests

The Kruskal–Wallis H Test can be used to a dataset when data are not normally distributed. The assumptions were stated in section 2.6.1.

3.4.1. Hypothesis test for distribution of LST

The frequency distribution of Built-up sub-classes shows that the shape of distributions among 17 sub-classes is not same for all and LST does not appear to be normally-distributed (Figure 3.4). Some of sub-classes are positively or negatively skewed. Although, zonal statistics of LST for these sub-classes showed median value differences among groups are small (STD differences are also small) and few groups have same median, the shape of the distributions are different. This heteroscedastic nature of data may not completely satisfy one assumption of Kruskal-Wallis test. However other two assumptions: Non-normal distribution, and one categorical variable and one ranked variable have met.

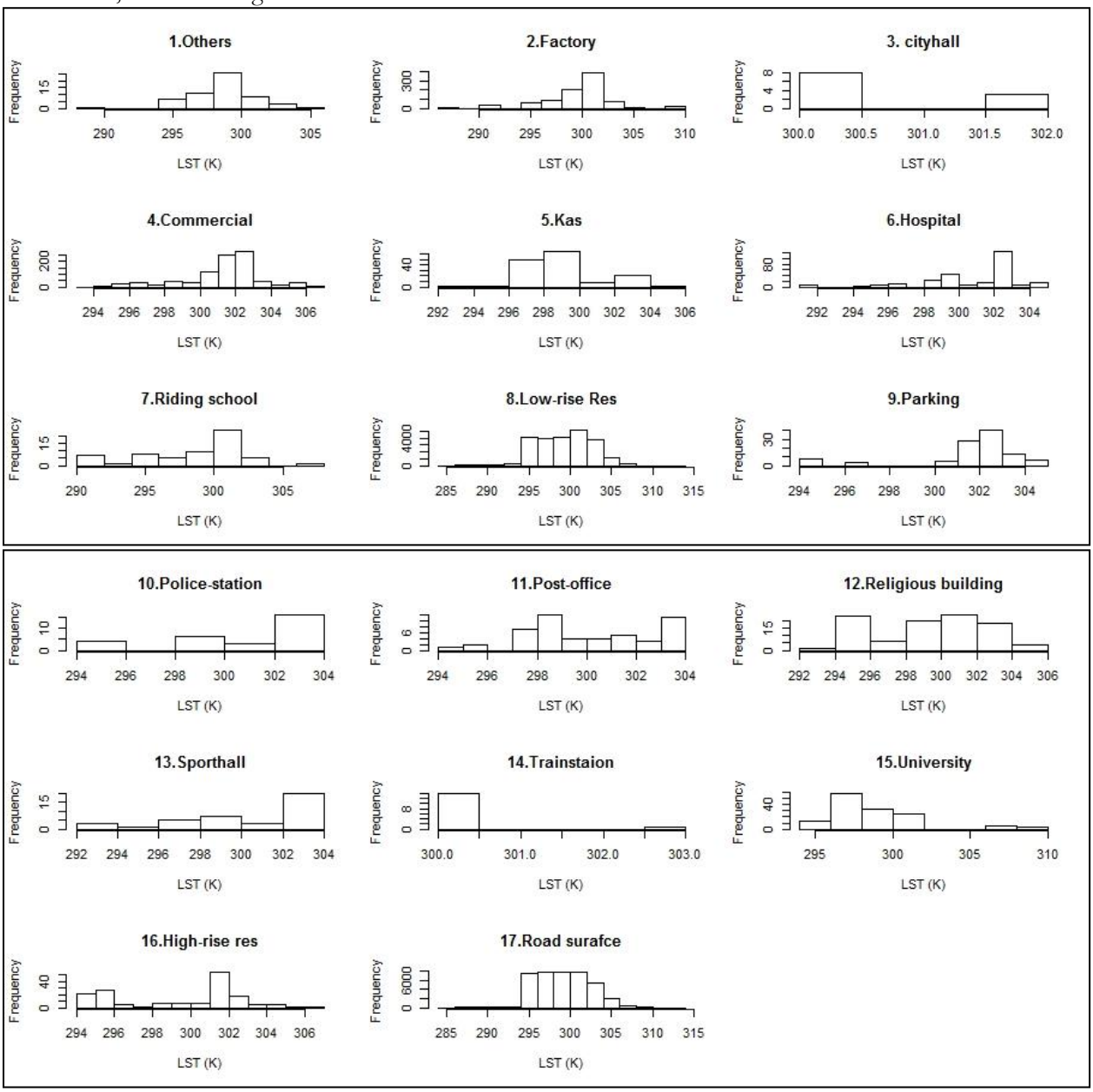

Figure 3.4 Histogram of LST for 17 Built-up sub-classes

Kruskal-Wallis rank sum test has applied to test LST distribution accors Built up sub-classes.

Kruskal-Wallis chi-squared = 726.7418, df = 16, p-value < 2.2e-16

As the Kruskal-Wallis Test statistics is highly significant ($\chi^{2\,(16)} = 726.7$, $p < 0.05$), the rejection of null hypothesis is possible with 95% confidence interval. The null hypothesis of the Kruskal–Wallis test is that the mean ranks of the groups are the same or, the medians of the groups are equal, but this is only true if the shape of the distribution in each group is the same. If the distributions are different, the Kruskal–Wallis test reject the null hypothesis even though the medians are the same (Fagerland & Sandvik, 2009).

The Tukey and Kramer *post-hoc* test calculate pairwise multiple comparisons between group levels these tests are sometimes referred to as Nemenyi-tests for multiple comparisons of (mean) rank sums of independent samples (Pohlert, 2014). The approach can be employed for equally as well as unequally sized samples without ties. The null hypothesis $H_0 : \bar{R}i = \bar{R}j$ will reject, if a critical absolute difference of mean rank sums exceed. The function *posthoc.kruskal.nemenyi.test()* in R package "**PMCMR"** used to perform the post-hoc test.

The test returns the lower triangle of the matrix that contains the p-values of the pairwise comparisons. The result of the Nemenyi post-hoc test for multiple joint samples is shown in the Table 3.12. A highlighted cell contains p-value, represent a pair which are significantly different ($p < 0.05$) from a non-highlighted one.

Table 3.12 Pairwise comparisons using Tukey and Kramer (Nemenyi) test with Tukey-Dist approximation for independent LST samples

P-value	Other	Factory	Cityhall	Comm H	Kas	Hosp.	Riding Sc	Lowrise	Parking	Police st	Postoffic	Reli buil	Sporthall	Train s	Universi	Highrise
Factory	0.935															
Cityhall	0.817	0.992														
Comm H	0.000	0.000	1.000													
Kas	1.000	0.226	0.714	0.000												
Hosp.	0.000	0.000	1.000	0.945	0.000											
Riding Sc	1.000	0.800	0.747	0.000	1.000	0.000										
Lowrise Res	0.998	0.656	0.959	0.000	0.736	0.000	0.983									
Parking	0.000	0.000	1.000	1.000	0.000	0.886	0.000	0.000								
Police st	0.205	0.674	1.000	1.000	0.061	1.000	0.132	0.332	0.994							
Postoffice	0.528	0.976	1.000	0.387	0.182	0.953	0.377	0.728	0.275	1.000						
Reli build	1.000	1.000	0.969	0.000	0.997	0.000	0.999	1.000	0.000	0.540	0.915					
Sporthall	0.403	0.917	1.000	0.863	0.135	0.999	0.277	0.596	0.689	1.000	1.000	0.815				
Train st	0.932	1.000	1.000	0.997	0.857	1.000	0.884	0.995	0.973	1.000	1.000	0.997	1.000			
University	1.000	0.025	0.541	0.000	1.000	0.000	1.000	0.184	0.000	0.019	0.055	0.919	0.042	0.692		
Highrise Res	0.991	1.000	0.991	0.000	0.798	0.000	0.958	1.000	0.000	0.706	0.980	1.000	0.930	1.000	0.358	
Road surface	1.000	0.000	0.859	0.000	0.999	0.000	1.000	0.000	0.000	0.111	0.295	1.000	0.229	0.956	0.849	0.932

The pairs of built-up classes whose LST are significantly different ($p<0.05$) from other pairs ($p>0.05$) is re-arranged into 2 groups. A group of 7 built-up classes, whose mean ranks are statistically significant ($p<0.05$) only when they make pairs with rest of the 10 classes, named as "Group 2". And others are as "Group 1".

Table 3.13 The reclassification of built-up classes based on pairwise rank test result from LST data

code	Group 1	Code	Group 2	Conclusion (from zonal statistics of both group)
1	Others	4	Commercial area	**Group2 > Group 1**
2	Factory	5	Kas	
3	Cityhall	6	Hospital	
7	Riding school	8	Lowrise Residential	
10	Policestation	9	Parking	
11	Post office	15	University	
12	Religious Building	16	Highrise Residential	
13	Sport-hall			
14	Train station			
17	Rail and road surface			

Table 3.13 shows list of the sub-classes in each group. It is worth to mention that the order among sub-classes in the group (Group1 and Group2) is not clear. The Post-hoc Kruskal.-Nemenyi test does not provide rank of individuals. The only conclusion can be made from this test (after rejecting null hypothesis) is which variable (built-up classes) or group of variables is significantly different from others. Here, Group 2 is significantly different from Group1. However, the order between two groups of built-up (LST of different built up can be ordered from warmer to cooler) can reveal from summary statistics. The reclassified Built-up using sub-classes that mentioned in Table 3.13 and its summary statistics of LST, and others have shown in Table 314. The difference between median LST of Group1 and Group2 is 0.6K and Mean is (0.4K). Although the difference is low, the order is Group2>Group1 as warmer to cooler shows a sign for the distribution of LST in the Built-up. The visualization of reclassified built-up is in Figure 3.5, where warmer area (Group2) refers as "warmer zone" and cooler (Group1) as "cooler zone".

Table 3.14 Zonal statistics of LST (top), Albedo, NDVI, NDBI and Emissivity for new built-up class: Group1 and Group 2

Class/LST	AREA	MIN	MAX	RANGE	MEAN	STD	VARIETY	MAJORITY	MINORITY	MEDIAN
Group 1	11437900	284.6	312.2	27.6	299.0	3.3	22.7	295.1	284.8	299.0
Group 2	8149730	285.4	312.2	26.8	299.4	3.3	20.7	295.1	287.1	299.6

Class/Albedo	AREA	MIN	MAX	RANGE	MEAN	STD	VARIET	MAJORITY	MINORITY	MEDIAN
Group1	11437900	0.093	0.469	0.376	0.207	0.029	0.246	0.191	0.093	0.204
Group2	8149730	0.086	0.424	0.338	0.205	0.027	0.232	0.194	0.094	0.202

Class/NDVI	AREA	MIN	MAX	RANGE	MEAN	STD	VARIETY	MAJORITY	MINORITY	MEDIAN
Group1	11437900	-0.019	0.829	0.848	0.580	0.140	0.691	0.726	-0.019	0.612
Group2	8149730	0.025	0.815	0.790	0.567	0.140	0.669	0.726	0.025	0.580

Class/NDBI	AREA	MIN	MAX	RANGE	MEAN	STD	VARIETY	MAJORITY	MINORITY	MEDIAN
Group1	19208300	-0.562	0.168	0.73	-0.22116	0.140648	0.631	-0.326	-0.562	-0.229
Group2	379350	-0.549	0.129	0.678	-0.21624	0.132626	0.598	-0.16	-0.549	-0.211

Class/Emissivity	AREA	MIN	MAX	RANGE	MEAN	STD	VARIETY	MAJORITY	MINORITY	MEDIAN
Group11	19208300	0.959	0.990	0.031	0.985	0.008	0.004	0.990	0.959	0.990
Group12	379350	0.959	0.990	0.031	0.982	0.008	0.004	0.990	0.959	0.980

The Table 3.14 also shows statistics of new Built-up class group1 (=cooler zone) and group2(= warmer zone) for all four parameters provides a quantitatively information about the relationship with LST.

For +0.6K changes of median LST, -0.002 median albedo, -0.032 median NDVI, -0.01 median emissivity and +0.018 median NDBI has changes between these two groups.

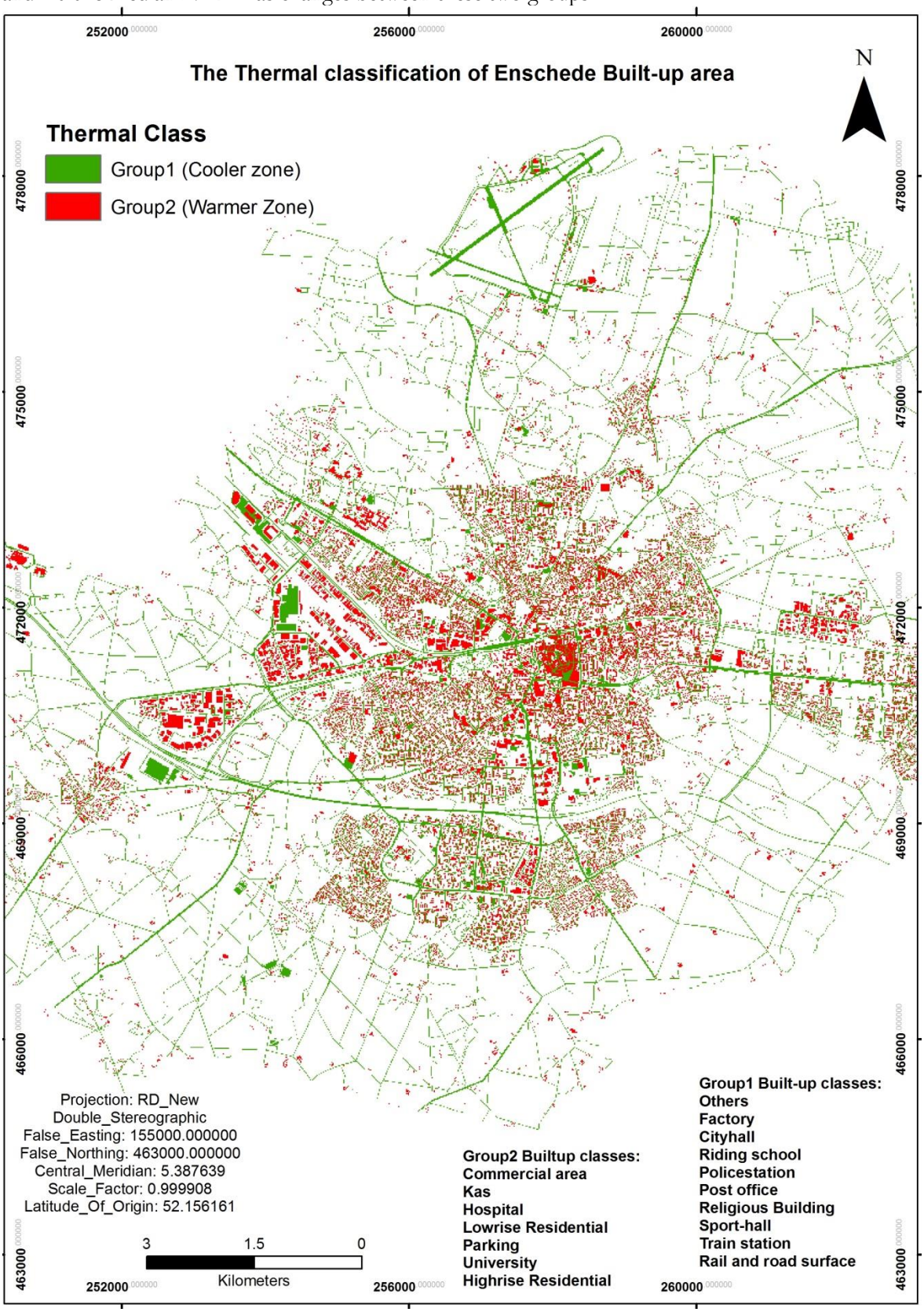

Figure 3.5 Built-up Reclassification; group2(= warmer zone) area consists of (i) Commercial (ii) Kas (iii) Hospitals (iv) Low-rise Residential (v) Parking (vi) University and (vii) High-rise Residential, and rest of the area (other 10 sub-classes) as group1 (=cooler zone)

3.4.2. Hypothesis test for distribution of Emissivity

The Emissivity histogram of Built-up sub-classes shows that the shape of distributions among 17 sub-classes is almost similar for all and emissivity distribution does not appear to be normally-distributed (Figure 3.6). But values are discrete. That seems the violation of one assumption of Kruskal-Wallis hypothesis rank test (Dependent variable should be ordinal or continuous (i.e., interval or ratio). The emissivity data is not appeared as continuous. Hence, it may not be appropriate to report the Kruskal-Wallis hypothesis results. However, the performed test results appeared as emissivity of two groups is significantly different (p=0.000).

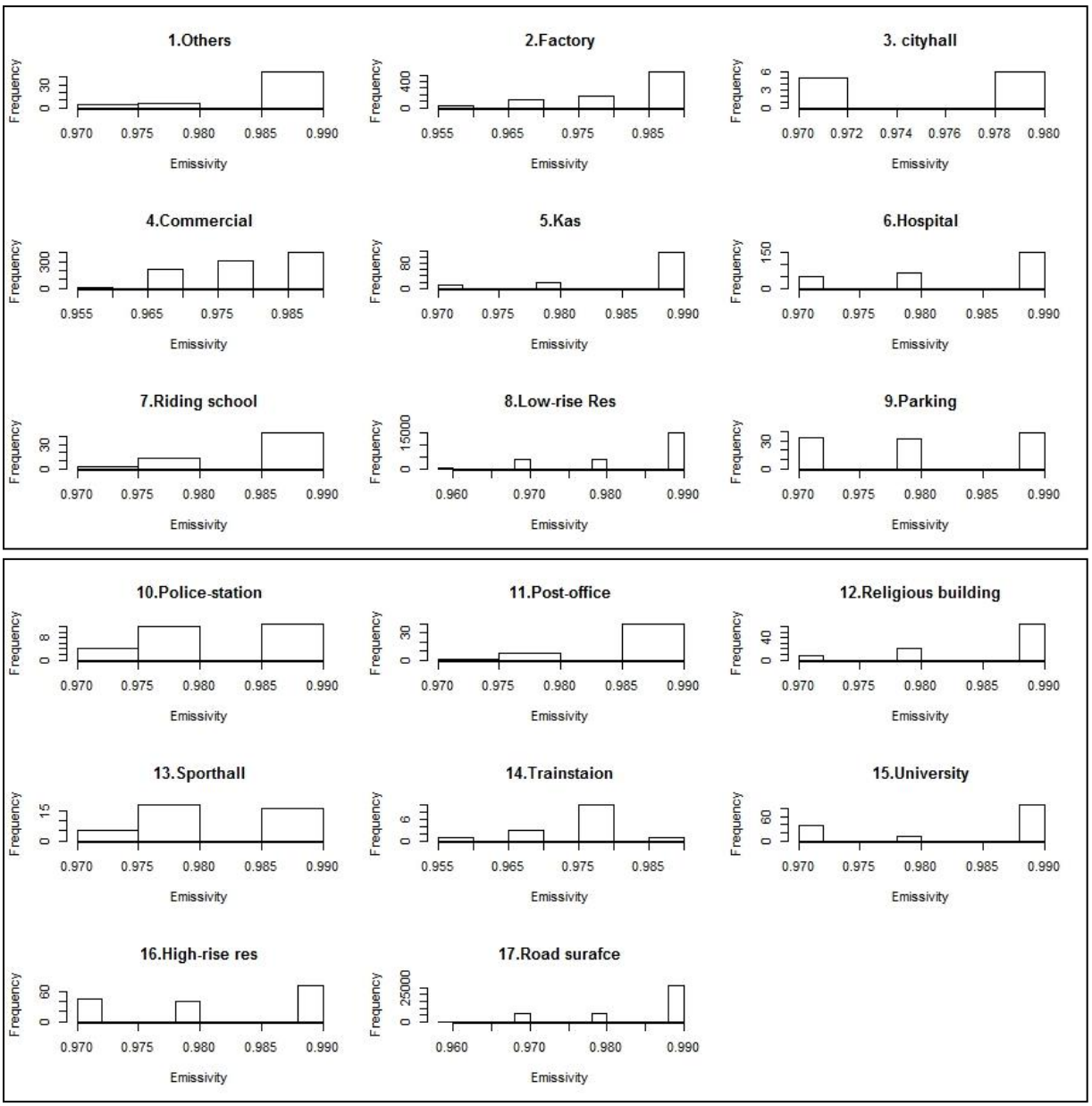

Figure 3.6 Histogram of Emissivity for 17 Built-up sub-classes

3.5. Multiple Linear Regression Model

Histograms in Figure 3.7 show the distribution of all variables. Albedo, LST and NDBI are symmetrically-distributed and Emissivity and NDVI distributions are skewed. The scatterplots in Figure 3.8 between LST and Albedo, Emissivity, NDVI, NDBI explains the association of LST with each variable. The relations of Albedo, NDVI, and NDBI with LST are somewhat linear but noisy with wide spread. The LST *vs.* Emissivity plot is hard to interpret since only few points are controlling the association. There is no way of knowing

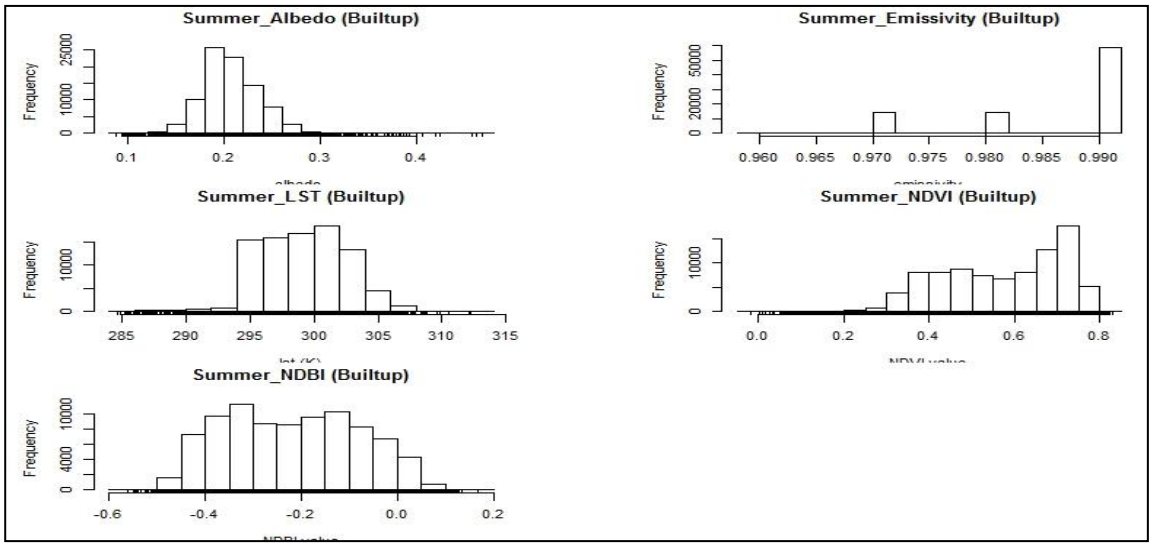

Figure 3.7 Histogram of Albedo, Emissivity, LST, NDVI, and NDBI in BUilt-up class

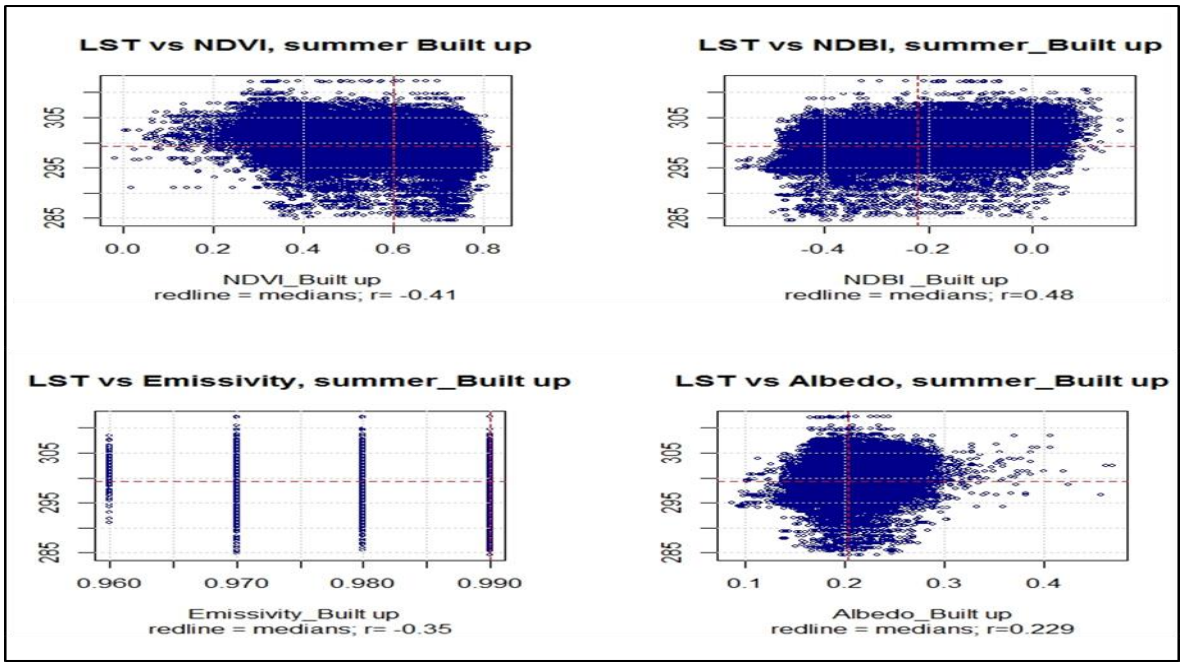

Figure 3.8 The scatter plots between LST and Albedo, Emissivity, NDBI, NDVI with medians (read line) and corelation coefficient (r).

intermediate points. In the built-up area, the corelation coefficient of LST and NDVI is -0.41, while the the corelation coefficient of LST and NDBI is 0.48. Liu & Zhang (2011) found similar results in urban heat analysis using ASTER images in Hong Kong. On the other hand, weaker corelations have found for

LST-Albedo (r=0.23) and LST-Emissivity (r=-0.35. The negative coefficient between LST and NDVI indicates that the impact of green land on urban heat island is negative, which means that the green land can weaken the urban heat island effect. In comparison, the positive correlation between LST and NDBI suggests that the build-up land can strengthen the urban heat island effect in this area.

To fit a suitable linear model it is important to check the collinearity among explanatory variables(Albedo, Emissivity, NDBI and NDVI). If two or more explanatory variables are highly correlated to each other, explaining response variable (LST) in terms of those explanatory variables may not explain better the response but increase complexity. One way of diagnosing multicollinearity is the pair-wise correlation coefficients among four explanatory variables. The results in Table 3.15 showed one pair have high positive (>0.5) collinearity (between NDVI and Emissivity) and another pair have high negative (<-0.5) collinearity (between NDVI and NDBI). The severity of multicollinearity problem can test by Variance Inflation Factor (VIF= 1/(1-R2)) calculation. VIF quantifies how much the variance of an estimated regression coefficient is increased because of collinearity. Table 3.16 shows the list of explanatory variables and the corresponding VIF values with rank.

Table 3.15 the Regression model summary

r-value	Albedo	Emissivity	NDBI	NDVI	LST
Albedo	1				
Emissivity	-0.41	1			
NDBI	0.38	-0.7	1		
NDVI	-0.37	0.73	-0.77	1	
LST	0.23	-0.35	0.48	-0.41	1

Table 3.16 VIF value of explanatory variables

Rank	Variables	VIF
4	NDVI	3.0
3	NDBI	2.8
2	Emissivity	2.5
1	Albedo	1.2

The VIF value of four variables is not too high to consider multicollinearity among them. The maximum variance of an estimated regression coefficient is 3.0, is less than 10, if we consider threshold VIF=10 as the indicator of severe collinearity (Jeffrey, 2007).

The stepwise backward regression start with the large model and then remove variables until the best model is found. In this case, model starts with all explanatory variables and based on the AIC values the best model has selected. The starting model has following form:

$$LST = f(NDVI + NDBI + Albedo + Emissivity)$$

Akaike's Information Criterion (AIC) compares models fitted by maximum likelihood to the same data. Smaller the AIC, better the fit. AIC found minimum when all four variables were considered. Hence all

variables have its contributing parts. The AIC value rank also indicates the relative importance of contributing variables. Higher AIC value found for variable NDBI than others (table not shown).

The result of final model is presented as summary in Table 3.17. Assessing only the p-values suggests that these four independent variables are equally statistically significant. The magnitude of the t-statistics (Table 3.17) provides a means to judge relative importance of the independent variables. The contribution of each independent variable's to the model has analyzed separately and will discuss in the next section.

Table 3.17 the Regression model summary

Independent variable	Regression coefficient	T- statistics	p-value	R^2 (adj)
Intercept	288.48	147.04	0.000	
Albedo	5.66	14.86	0.000	
Emissivity	13.31	6.62	0.000	0.237
NDBI	9.56	80.33	0.000	
NDVI	-2.54	-20.87	0.000	

The adjusted R^2 in table 3.17 shows that the final regression model explains about 23.7% of the overall variability in LST with NDVI, NDBI, Albedo, and Emissivity. P-value (<0.05) is highly significant for all predictors. The F-statistic indicates that the p-value (probability that rejecting the null hypothesis would be an error) is almost zero, so rejecting the null hypothesis (no effect for any of four predictors on LST) is possible Table 3.18.

Table 3.18 Regression model hypothesis result

Predictor	P	Null Hyp.	Decision	Conclusion
Intercept	0.000	$\beta_0 = 0$	Reject H_0	Intercept and all predictors do significantly contribute to predict LST
Albedo	0.000	$\beta_1 = 0$	Reject H_0	
Emissivity	0.000	$\beta_2 = 0$	Reject H_0	
NDBI	0.000	$\beta_3 = 0$	Reject H_0	
NDVI	0.000	$B_4 = 0$	Reject H_0	

The LST prediction equation obtained from regression analysis is

$$LST = 5.66 * Albedo + 13.31 * Emissivity - 2.54 * NDVI + 9.56 * NDBI + 288.48 \quad (3.1)$$

The R-squared value measures how close the data are to the fitted regression line. In general, the higher the R-squared, the better the model fit. A fitted model with low R-squared value is not always bad. According to Jim (2013) the limitations of R-squared are (1) it cannot determine whether the coefficient

estimates and predictions are biased, which can be assess by the residual plots. (2) R-squared does not indicate whether a regression model is adequate. A good model can have a low R-squared value, or a high R-squared value for a model that does not fit the data. A high R-squared value is required when the purpose of the model is for precise prediction. How high the R-squared should be that depends on requirement for the width of a prediction interval. On the other hand, low R-squared value doesn't affect the interpretation of significant variables. Statistically significant predictors explained how changes in the predictor values are associated with changes in the response value. Regardless of the R-squared, the significant coefficients still represent the mean change in the response for one unit of change in the predictor.

The regression diagnostics plots (Figure 3.10) and histogram of the regression residuals (Figure 3.9) will visualize discussing other assumptions of regression model. The histogram of residuals is somewhat peaked and the highest residuals are too low. The median residual is slightly biased (-0.02). However, the range is quite high (+/- 15K). The result of Shapiro-Wilk test confirms (p-value is almost zero) that the residuals is normality-distributed.

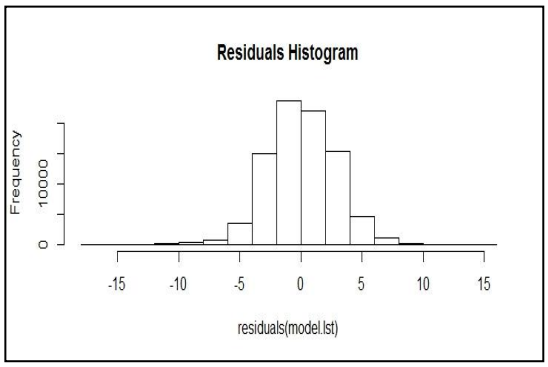

Figure 3.9 Frequency distribution of residuals (K)

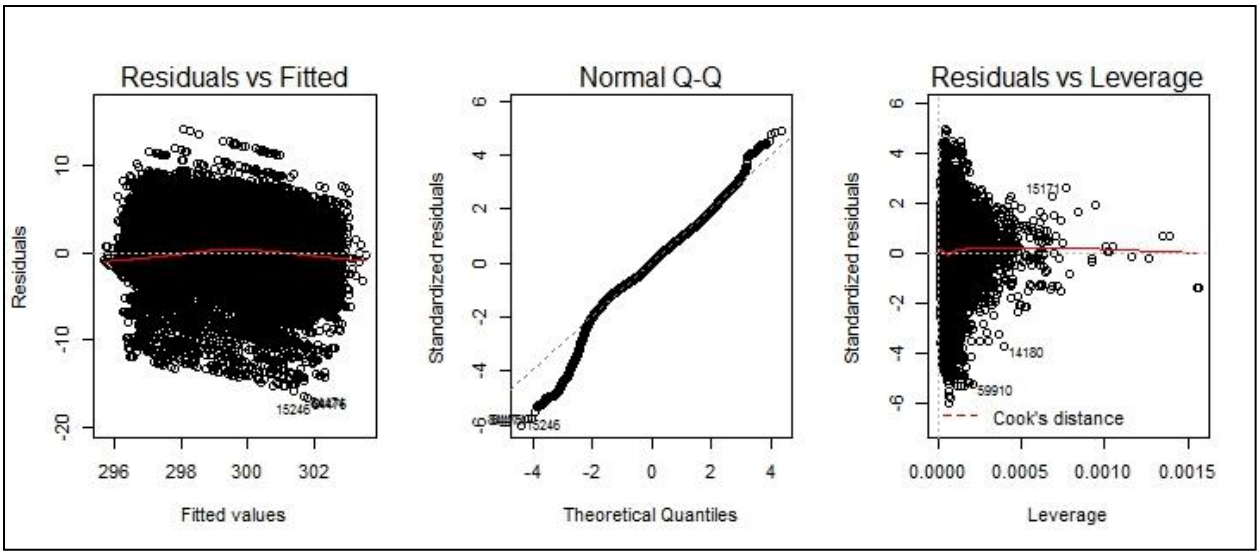

Figure 3.10 Regression diagnostic plots

The plot of residuals *vs.* fitted values (plot 1 in Figure 3.10) does not show any relation between these. The smooth horizontal red line (ideally should go through at 0) provides evidence that residuals do not have any trend. The variance of the residuals is not always equal across the range of the predictor. That means, they may not be homoscedastic, which is one of the assumption for linear regression model – may not

satisfied. Deviation at both tails in the normal Q-Q plot also confirms the normality of residuals. The residual *vs.* leverage plot is useful to check whether there are any high leverage points or highly influential points. Leverage measures the overall inuence of a single observation on the predictions.

3.6. Relative importance of Independent Variables in a multiple regression model

The quantification of each independent variable's contribution to a multiple regression model refers Relative Importance or Commonality Effect analysis in regression model where, each regressor's contribution is just the R^2 from univariate regression, and all univariate R^2-values add up to the full model R^2 (Grömping, 2006).

Nimon *et. al.,* (2008) introduced R-package named "**MBESS"** and **"yhat"** to compute commonality coefficients. The contributions of unique and common elements are separated by partitioning R^2-value from a multiple regression model.

Table 3.19 represents the partitioning of regression effect. The total of the commonality coefficients (CC) is equal to the total R^2 from the multiple regression model (*i.e.,* 0.2372 or 23.72% of total variance). The individual entries in the table shows how much variance is explained by unique effects (each independent variable) , first-order common effects (each combination of two independent variables), second-order common effects (each combination of three independent variables), and so forth, as well as which coefficients contribute most to the regression effect. The highest unique contribution is from NDBI 23.85% of total R^2 (0.0566 of 0.2372) and highest common contribution from Emissivity, NDVI, and NDBI is 32.71% of total R^2 (0.0776 of 0.2372). On the other hand, Albedo has the least effect as a unique contributor explained only less than 1% of total R^2, followed by unique Emissivity effect. Albedo, Emissivity, NDVI and NDBI (17.56%) ; Emissivity, NDVI and NDBI (32.71%) ; NDVI and NDBI (18.74%); and NDBI (23.85%) explained 93% of total R^2.

Table 3.20 provides another view of commonality effects. The unique effect for each predictor is tabularized, as well as the total of all common effects for which the predictor is involved. Total (in Table 3.20) can be compared alongside the unstandardized weights resulting from the multiple regression to add another layer of consideration when determining which variables are important to a regression equation. A graphical representation of Commonality Effect analysis in regression model is shown in Figure 3.14.

Table 3.19 List of commonality coefficients (CC) and the per cent of variance (R2) for each effect. Full model R2 = 0.2372

Effects	**Commonality Coefficient (CC)**	**% Total**
Unique to Albedo	0.0019	0.82
Unique to Emissivity	0.0004	0.16
Unique to NDVI	0.0038	1.61
Unique to NDBI	0.0566	23.85
Common to Albedo, and Emissivity	-0.0003	-0.11
Common to Albedo, and NDVI	0.0002	0.08
Common to Emissivity, and NDVI	-0.0003	-0.15
Common to Albedo, and NDBI	0.0026	1.12
Common to Emissivity, and NDBI	0.0023	0.97
Common to NDVI, and NDBI	0.0444	18.74
Common to Albedo, Emissivity, and NDVI	0.0005	0.21
Common to Albedo, Emissivity, and NDB	0.0023	0.98

Common to Albedo, NDVI, and NDBI	0.0035	1.46
Common to Emissivity, NDVI, and NDBI	0.0776	32.71
Common to Albedo, Emissivity, NDVI, and NDBI	0.0416	17.56
Total	**0.2372**	**100.00**

Table 3.20 Unique, common and total effects for each independent variable

	Unique	Common	Total	% of R^2 (=Total/ R^2)
Albedo	0.0019	0.0505	0.0524	22.0
Emissivity	0.0004	0.1237	0.1241	52.3
NDVI	0.0038	0.1675	0.1713	72.1
NDBI	0.0566	0.1743	0.2309	97.4

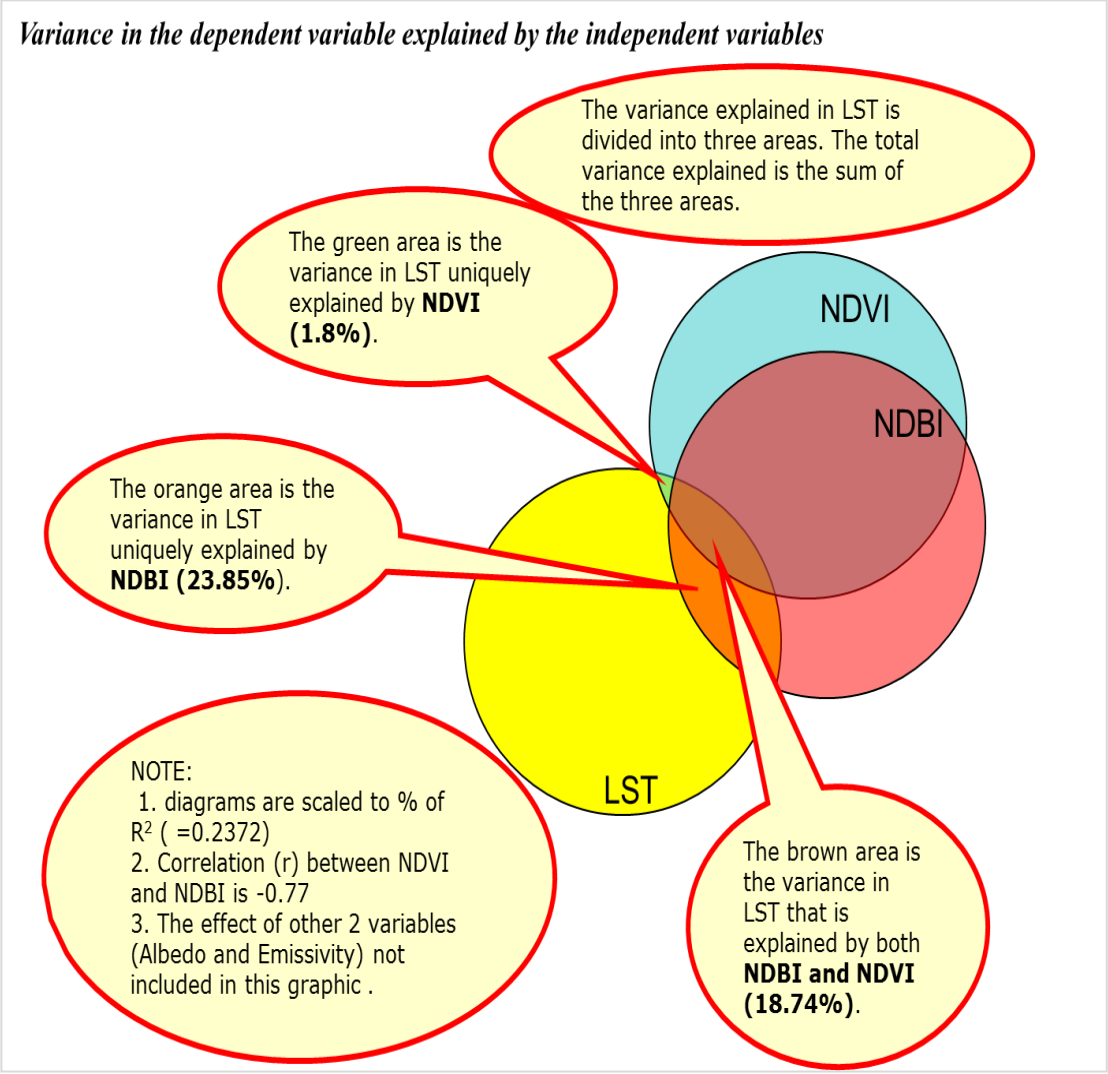

Figure 3.11 Venn diagram describes the partitioning of R2 to the contributing variables in regression model

This analysis showed that the majority of the regression effect was explained by a small subset of unique and common effects. It further showed that the predictors NDBI and NDVI shared a significant amount of variance with the regression effect.

4. CONCLUSIONS AND RECOMMENDATIONS

The Land Surface Temperature (LST) retrieved from ASTER image has analysed to investigate surface temperature distributions in the Enschede Municipality, The Netherlands. Land surface parameters like Albedo, Emissivity and satellite based indices NDVI and NDBI also analysed to establish a relationship with LST. A detail Built-up map with 17 sub-classes used to identify warmer or cooler surfaces on a clear-sky summer day. Results showed that a group of area is significantly different than others. The median LST difference between these 2 groups is 0.6k. Based on the LST distribution in the Built-up area, a thermal map of urban surface is produced for the study area which may be useful to identify potential over-heating area. On the other hand, relation between LST and land surface parameters is also found significant. Although only 23.7% of LST variation was explained by the parameters, the relationship has found statistically significant. The NDBI is appeared as an important factor to explain the LST variability, along with NDVI and Emissivity, NDBI explains 97% of LST variations. The Visual interpretations between LST and other parameters showed LST is positively associated with NDBI and negatively with NDVI, Emissivity and albedo. However, albedo appears as has almost no or weak influence on LST. The specific answers to the proposed hypothesis are given below:

3 hypothesis test concludes:

- The median LST is significantly different for some of Built-up classes according to Kruskal-Wallis rank sum test. LST of the following areas of Enschede: Commercial, Kas, Hospitals, Low-rise Residential, Parking, University and High-rise Residential, are higher than other areas. On the other hand, the industrial (factory), Cityhall and road surface area appeared as cooler compare to the Commercial area, parking or from university area.
- The processed emissivity data has a very short ranges and are not continuous over the study area, which implies the rank test may not be appropripate with this data.
- Intercept and all predictors (NDBI, NBVI, Emissivity and Albedo) do significantly contribute to predict LST in the multiple regression model:

  $$LST = 5.66 * Albedo + 13.31 * Emissivity - 2.54 * NDVI + 9.56 * NDBI + 288.48$$

  23.7% of total variability of LST is explained by the model. Predictors NDBI and NDVI shared a significant amount of variance with the regression effect.

A drawback with this study is the derivation of Emissivity. It was calculated from NDVI and surface roughness information that are more applicable for vegetation surfaces. A constant value of roughness height for the Built-up area is considered in the emissivity calculation, which was done using ILWIS SEBS tools. This SEBS model is more suitable for water, vegetation and agriculture related research over urban study.

A more accurate emissivity derivation method is TES (Temperature Emissivity Separation) algorithm, which is also a LST estimation method. TES is a more complex method but with high accuracy of LST. The implementation of TES method to derive LST and emissivity would require allocating more time on image pre-processing. On the other hand, using the Split Window method for LST derivation was considered that it may not affect the main purpose of the study, as the RMSE of Split-window method is about 1K.

Further research is possible based on this study. An application of TES algorithm, or use of ASTER high level product to obtain processed emissivity map should be useful to address emissivity distribution in the urban area.

LIST OF REFERENCES

Abrams, M. (2001). *ASTER User Handbook Version 2*. Pasadena, CA.

Adam, L., & Lund, M. (2013). How to perform a Multiple Regression Analysis in SPSS Statistics | Laerd Statistics. *Lund Research Ltd*. Retrieved May 27, 2015, from https://statistics.laerd.com/spss-tutorials/multiple-regression-using-spss-statistics.php

Akbari, H., Bell, R., Brazel, T., Cole, D., Estes, M., Heisler, G., Zalph, B. (2008). *Reducing Urban Heat Islands : Compendium of Strategies Urban Heat Island Basics*. Retrieved from http://www.epa.gov/heatisland/resources/compendium.htm

Anniballe, R., Bonafoni, S., & Pichierri, M. (2014). Spatial and temporal trends of the surface and air heat island over Milan using MODIS data. *Remote Sensing of Environment*, *150*, 163–171. doi:10.1016/j.rse.2014.05.005

Arnfield, A. J. (2003). Two decades of urban climate research: a review of turbulence, exchanges of energy and water, and the urban heat island. *International Journal of Climatology*, *23*(1), 1–26. doi:10.1002/joc.859

Asimakopoulos, D. N., Assimakopoulos, V. D., Chrisomallidou, N., Klitsikas, N., Mangold, D., Michel, P., Tsangrassoulis, A. (2011). *Energy and climate in the urban built environment*. (M. Santamouris, Ed.). Routledge.

Beta Paramitaa, H. F. (2012). Study on The Affect of Aspect Building Form and Layout Case study : Honjo Nishi Danchi, Yahatanishi, Kitakyushu - Fukuoka. In *The 3rd International Conference on Sustainable Future for Human Security SUSTAIN*. Retrieved from file:///C:/Users/acer.acer-PC/Downloads/EnE_28 betaparamita.pdf

Borbora, J., & Das, A. K. (2014). Summertime Urban Heat Island study for Guwahati City, India. *Sustainable Cities and Society*, *11*, 61–66. doi:10.1016/j.scs.2013.12.001

Bottyán, Z., Kircsi, A., Szegedi, S., & Unger, J. (2005). The relationship between built-up areas and the spatial development of the mean maximum urban heat island in Debrecen, Hungary. *International Journal of Climatology*, *25*(3), 405–418. doi:10.1002/joc.1138

Brandsma, T., Konnen, G. P., & Wessels, H. R. A. (2003). Empirical estimation of the effect of urban heat advection on the temperature series of De Bilt (The Netherlands). *International Journal of Climatology*, *23*(7), 829–845. doi:10.1002/joc.902

Brest, C. L. (1987). Seasonal Albedo of an Urban/Rural Landscape from Satellite Observations. *Journal of Climate and Applied Meteorology*, *26*(9), 1169–1187. doi:10.1175/1520-0450(1987)026<1169:SAOAUL>2.0.CO;2

Busato, F., Lazzarin, R. M., & Noro, M. (2014). Three years of study of the Urban Heat Island in Padua: Experimental results. *Sustainable Cities and Society*, *10*, 251–258. doi:10.1016/j.scs.2013.05.001

Chatterjee, S., & S., H. A. (2012). *Regression Analysis by Example* (5th ed.). Wiley. Retrieved from http://eu.wiley.com/WileyCDA/WileyTitle/productCd-0470905840.html

Chen, X.-L., Zhao, H.-M., Li, P.-X., & Yin, Z.-Y. (2006). Remote sensing image-based analysis of the relationship between urban heat island and land use/cover changes. *Remote Sensing of Environment*, *104*(2), 133–146. doi:10.1016/j.rse.2005.11.016

Christen, A., & Vogt, R. (2004). Energy and radiation balance of a central European city. *International Journal of Climatology*, *24*(11), 1395–1421. doi:10.1002/joc.1074

Chrysoulakis, N. (2003). Estimation of the all-wave urban surface radiation balance by use of ASTER multispectral imagery and in situ spatial data. *Journal of Geophysical Research*, *108*(D18), 4582. doi:10.1029/2003JD003396

Chrysoulakis, N., Feigenwinter, C., Triantakonstantis, D., Penyevskiy, I., Tal, A., Parlow, E., … Marconcini, M. (2014). A Conceptual List of Indicators for Urban Planning and Management Based on Earth Observation. *ISPRS International Journal of Geo-Information*, *3*(3), 980–1002. doi:10.3390/ijgi3030980

Cohen, P., Potchter, O., & Matzarakis, A. (2013). Human thermal perception of Coastal Mediterranean outdoor urban environments. *Applied Geography*, *37*, 1–10. doi:10.1016/j.apgeog.2012.11.001

Essa, W., van der Kwast, J., Verbeiren, B., & Batelaan, O. (2013). Downscaling of thermal images over urban areas using the land surface temperature–impervious percentage relationship. *International Journal of Applied Earth Observation and Geoinformation*, *23*, 95–108. doi:10.1016/j.jag.2012.12.007

Fagerland, M. W., & Sandvik, L. (2009). The Wilcoxon-Mann-Whitney test under scrutiny. *Statistics in Medicine*, *28*(10), 1487–1497. doi:10.1002/sim.3561

GHO. (2014). WHO | Urban population growth. World Health Organization. Retrieved September 2, 2014, from http://www.who.int/gho/urban_health/situation_trends/urban_population_growth_text/en

Gowda, P. H., Chávez, J. L., Howell, T. a., Marek, T. H., & New, L. L. (2008). Surface Energy Balance Based Evapotranspiration Mapping in the Texas High Plains. *Sensors*, *8*(8), 5186–5201. doi:10.3390/s8085186

Grimmond, C. S. B. (2005). Progress in measuring and observing the urban atmosphere. *Theoretical and Applied Climatology*, *84*(1-3), 3–22. doi:10.1007/s00704-005-0140-5

Grömping, U. (2006). Relative importance for linear regression in R: the package relaimpo. *Journal Of Statistical Software*, *17*(1), 139–147. Retrieved from http://www.jstatsoft.org/v17/a01/paper

Holzman, M. E., Rivas, R., & Piccolo, M. C. (2014). Estimating soil moisture and the relationship with crop yield using surface temperature and vegetation index. *International Journal of Applied Earth Observation and Geoinformation*, *28*, 181–192. doi:10.1016/j.jag.2013.12.006

Jeffrey, W. B. (2007). Identifying Multicollinearity in Multiple Regression. Retrieved May 27, 2015, from http://www.researchconsultation.com/multicollinearity-regression-spss-collinearity-diagnostics-vif.asp

Jim, F. (2013). Regression Analysis: How Do I Interpret R-squared and Assess the Goodness-of-Fit? *Minitab Inc.* Retrieved May 27, 2015, from http://blog.minitab.com/blog/adventures-in-statistics/regression-analysis-how-do-i-interpret-r-squared-and-assess-the-goodness-of-fit

Jin, M., Dickinson, R. E., & Zhang, D. (2005). The Footprint of Urban Areas on Global Climate as Characterized by MODIS. *Journal of Climate*, *18*(10), 1551–1565. doi:10.1175/JCLI3334.1

Kato, S., & Yamaguchi, Y. (2005). Analysis of urban heat-island effect using ASTER and ETM+ Data: Separation of anthropogenic heat discharge and natural heat radiation from sensible heat flux. *Remote Sensing of Environment*, *99*(1-2), 44–54. doi:10.1016/j.rse.2005.04.026

Kato, S., & Yamaguchi, Y. (2007). Estimation of storage heat flux in an urban area using ASTER data. *Remote Sensing of Environment*, *110*(1), 1–17. doi:10.1016/j.rse.2007.02.011

Kruskal, W. H., & Wallis, W. A. (1952). Use of Ranks in One-Criterion Variance Analysis. *Journal of the American Statistical Association*, *47*(260), 583–621. doi:10.1080/01621459.1952.10483441

Lee, S.-H., & Baik, J.-J. (2010). Statistical and dynamical characteristics of the urban heat island intensity in Seoul. *Theoretical and Applied Climatology*, *100*(1-2), 227–237. doi:10.1007/s00704-009-0247-1

Lee, T.-W., Choi, H. S., & Lee, J. (2014). Generalized Scaling of Urban Heat Island Effect and Its Applications for Energy Consumption and Renewable Energy. *Advances in Meteorology*, *2014*, 1–5. doi:10.1155/2014/948306

Lee, T.-W., & Ho, A. (2010). Scaling of the urban heat island effect based on the energy balance: nighttime minimum temperature increase vs. urban area length scale. *Climate Research*, *42*(3), 209–216.

Liang, S. (2000). Narrowband to broadband conversions of land surface albedo I: Algorithms. *Remote Sensing of Environment*, *76*, 213–238. Retrieved from http://www.sciencedirect.com/science/article/pii/S0034425700002054

Liu, L., & Zhang, Y. (2011). Urban Heat Island Analysis Using the Landsat TM Data and ASTER Data: A Case Study in Hong Kong. *Remote Sensing*, *3*(12), 1535–1552. doi:10.3390/rs3071535

Lokoshchenko, M. a. (2014). Urban "heat island" in Moscow. *Urban Climate*, 1–13. doi:10.1016/j.uclim.2014.01.008

Lu, L., Venus, V., Skidmore, A., Wang, T., & Luo, G. (2011). Estimating land-surface temperature under clouds using MSG/SEVIRI observations. *International Journal of Applied Earth Observation and Geoinformation*, *13*(2), 265–276. doi:10.1016/j.jag.2010.12.007

Mallick, J., Kant, Y., Bharath, B. D., Atzberger, C., & Kerle, N. (2009). Satellite-based analysis of the role of land use/land cover and vegetation density on surface temperature regime of Delhi, India. *Journal of the Indian Society of Remote Sensing*, *37*(2), 201–214. Retrieved from http://link.springer.com/article/10.1007/s12524-009-0030-x

Maurer, J. (2002). Retrieval of surface albedo from space. Retrieved October 23, 2014, from http://www2.hawaii.edu/~jmaurer/albedo/

McDonald, J. H. (2014). Kruskal–Wallis test - Handbook of Biological Statistics. Retrieved May 26, 2015, from http://www.biostathandbook.com/kruskalwallis.html

Mills, G. (2007). Luke Howard, Tim Oke and the study of urban climates. *Weather*, *63*, 153–157.

Mitraka, Z., Chrysoulakis, N., Kamarianakis, Y., Partsinevelos, P., & Tsouchlaraki, A. (2012). Improving the estimation of urban surface emissivity based on sub-pixel classification of high resolution satellite imagery. *Remote Sensing of Environment*, *117*, 125–134. doi:10.1016/j.rse.2011.06.025

Nimon, K., Lewis, M., Kane, R., & Haynes, R. M. (2008). An R package to compute commonality coefficients in the multiple regression case: an introduction to the package and a practical example. *Behavior Research Methods*, *40*(2), 457–466. doi:10.3758/BRM.42.1.363

Offerle, B., Grimmond, C. S. B., & Oke, T. R. (2003). Parameterization of Net All-Wave Radiation for Urban Areas. *Journal of Applied Meteorology*, *42*(8), 1157–1173. doi:10.1175/1520-0450(2003)042<1157:PONARF>2.0.CO;2

Oke, T. R. (1981). Canyon geometry and the nocturnal urban heat island: Comparison of scale model and field observations. *Journal of Climatology*, *1*(3), 237–254. doi:10.1002/joc.3370010304

Oke, T. R. (1988). The urban energy balance. *Progress in Physical Geography*, *12*(4), 471–508. doi:10.1177/030913338801200401

Parlow, E., Vogt, R., & Feigenwinter, C. (2014). The urban heat island of Basel – seen from different perspectives. *Journal of the Geographical Society of Berlin*, *145*(1), 96–110. doi:10.12854/erde-145-8

Pohlert, T. (2014). The Pairwise Multiple Comparison of Mean Ranks Package (PMCMR). *R Package*, 1–9.

Qiao, Z., Tian, G., & Xiao, L. (2013). Diurnal and seasonal impacts of urbanization on the urban thermal environment: A case study of Beijing using MODIS data. *ISPRS Journal of Photogrammetry and Remote Sensing*, *85*, 93–101. doi:10.1016/j.isprsjprs.2013.08.010

Qin, Z., Li, W., Gao, M., & Zhang, H. (2006). An algorithm to retrieve land surface temperature from ASTER thermal band data for agricultural drought monitoring, *6359*, 63591F–63591F–8. doi:10.1117/12.689307

Rizwan, A. M., Dennis, L. Y. C., & Liu, C. (2008). A review on the generation, determination and mitigation of Urban Heat Island. *Journal of Environmental Sciences*, *20*(1), 120–128. doi:10.1016/S1001-0742(08)60019-4

Rossiter, D. G. (2012). *Introduction to Correlation and Regression*. Enschede.

Ryu, Y.-H., & Baik, J.-J. (2012). Quantitative Analysis of Factors Contributing to Urban Heat Island Intensity. *Journal of Applied Meteorology and Climatology*, *51*(5), 842–854. doi:10.1175/JAMC-D-11-098.1

Statline, C. (2015). CBS StatLine - Bevolkingsontwikkeling; regio per maand. Retrieved May 31, 2015, from http://statline.cbs.nl/StatWeb/publication/?DM=SLNL&PA=37230ned&D1=17&D2=57-100&D3=l&LA=EN&HDR=G2&STB=G1,T&VW=T

Steeneveld, G. J., Koopmans, S., Heusinkveld, B. G., van Hove, L. W. a., & Holtslag, a. a. M. (2011). Quantifying urban heat island effects and human comfort for cities of variable size and urban

morphology in the Netherlands. *Journal of Geophysical Research*, *116*(D20), D20129. doi:10.1029/2011JD015988

Streutker, D. R. (2002). A remote sensing study of the urban heat island of Houston, Texas. *International Journal of Remote Sensing*, *23*(13), 2595–2608. doi:10.1080/01431160110115023

Sun, D., & Yu, Y. (2013). Land Surface Temperature (LST) Retrieval from GOES Satellite Observations. In J. Qu, A. Powell, & M. V. K. Sivakumar (Eds.), *Satellite-based Applications on Climate Change*. Dordrecht: Springer Netherlands. doi:10.1007/978-94-007-5872-8

Taha, H. (1997). Urban climates and heat islands: albedo, evapotranspiration, and anthropogenic heat. *Energy and Buildings*, *25*(2), 99–103. doi:10.1016/S0378-7788(96)00999-1

Taha, H., Sailor, D., & Akbari, H. (1992). *High-albedo materials for reducing building cooling energy use*. Berkeley, CA. doi:10.2172/7000986

Tang, H., & Li, Z.-L. (2014). Land Surface Temperature Retrieval from Thermal Infrared Data. In *Quantitative Remote Sensing in Thermal Infrared*. Berlin, Heidelberg: Springer Berlin Heidelberg. doi:10.1007/978-3-642-42027-6

Tian, H., Wen, J., Wang, C., Liu, R., & Lu, D. (2012). Effect of pixel scale on evapotranspiration estimation by remote sensing over oasis areas in north-western China. *Environmental Earth Sciences*, *67*(8), 2301–2313. doi:10.1007/s12665-012-1677-0

Tol, C. van der, & Parodi, G. N. (2012). Guidelines for Remote Sensing of Evapotranspiration. In D. A. Irmak (Ed.), *Evapotranspiration – Remote Sensing and Modeling*. InTech. Retrieved from http://www.intechopen.com/books/evapotranspiration-remote-sensing-and- modeling/guidelines-for-remote-sensing-of-evapotranspiration

Van Hove, L. W. A., Steeneveld, G. J., C.M.J. Jacobs, B. G., Heusinkveld, J. A., Elbers, E. J., & Moors Holtslag, A. A. M. (2011). *Exploring the Urban Heat Island Intensity of Dutch cities*. Wageningen.

Voogt, J. A., & Oke, T. R. (1997). Complete urban surface temperatures. *Journal of Applied Meteorology*, *36*, 1117–1132. doi:10.1175/1520-0450(1997)036<1117:CUST>2.0.CO;2

Voogt, J. A., & Oke, T. R. (2003). Thermal remote sensing of urban climates. *Remote Sensing of Environment*, *86*(3), 370–384. doi:10.1016/S0034-4257(03)00079-8

Wang, K., Wang, J., Wang, P., Sparrow, M., Yang, J., & Chen, H. (2007). Influences of urbanization on surface characteristics as derived from the Moderate-Resolution Imaging Spectroradiometer: A case study for the Beijing metropolitan area. *Journal of Geophysical Research*, *112*(D22), D22S06. doi:10.1029/2006JD007997

Weng, Q. (2009). Thermal infrared remote sensing for urban climate and environmental studies: Methods, applications, and trends. *ISPRS Journal of Photogrammetry and Remote Sensing*, *64*(4), 335–344. doi:10.1016/j.isprsjprs.2009.03.007

Weng, Q., Liu, H., & Lu, D. (2007). Assessing the effects of land use and land cover patterns on thermal conditions using landscape metrics in city of Indianapolis, United States. *Urban Ecosystems*, *10*(2), 203–219. doi:10.1007/s11252-007-0020-0

Weng, Q., & Lu, D. (2008). A sub-pixel analysis of urbanization effect on land surface temperature and its interplay with impervious surface and vegetation coverage in Indianapolis, United States. *International Journal of Applied Earth Observation and Geoinformation*, *10*(1), 68–83. doi:10.1016/j.jag.2007.05.002

Weng, Q., Lu, D., & Schubring, J. (2004). Estimation of land surface temperature–vegetation abundance relationship for urban heat island studies. *Remote Sensing of Environment*, *89*(4), 467–483. doi:10.1016/j.rse.2003.11.005

Xiao, R., Weng, Q., Ouyang, Z., Li, W., Schienke, E. W., & Zhang, Z. (2008). Land Surface Temperature Variation and Major Factors in Beijing, China. *Photogrammetric Engineering & Remote Sensing*, *74*(4), 451–461. doi:10.14358/PERS.74.4.451

Yap, D. (1975). Seasonal excess urban energy and the nocturnal heat island — Toronto. *Archives for Meteorology, Geophysics and Bioclimatology Series B*, *23*(1-2), 69–80. doi:10.1007/BF02247308

Yuan, F., & Bauer, M. E. (2007). Comparison of impervious surface area and normalized difference vegetation index as indicators of surface urban heat island effects in Landsat imagery. *Remote Sensing of Environment*, *106*(3), 375–386. doi:10.1016/j.rse.2006.09.003

Zakšek, K., & Oštir, K. (2012). Downscaling land surface temperature for urban heat island diurnal cycle analysis. *Remote Sensing of Environment*, *117*, 114–124. doi:10.1016/j.rse.2011.05.027

Zhang, Y., Balzter, H., & Wu, X. (2013). Spatial–temporal patterns of urban anthropogenic heat discharge in Fuzhou, China, observed from sensible heat flux using Landsat TM/ETM+ data. *International Journal of Remote Sensing*, *34*(4), 1459–1477. doi:10.1080/01431161.2012.718465

Zhang, Y., Wang, X., & Chen, Y. (2012). An Improved 6S Code for Atmospheric Correction Based on Water Vapor Content. *Advances in Remote Sensing*, *2012*(June), 14–18. Retrieved from http://www.scirp.org/journal/PaperInformation.aspx?paperID=20390

5. APPENDIX

5.1. Appendix –A

Table 5.1 Acquired ASTER image characteristics provided in metadata with the image

Items	Descriptions
Instrument Name	Advanced Spaceborne Thermal Emission and Reflection Radiometer
Platform Name	First EOS Polar Orbiting Satellite, 10:30 AM Descending Equator Crossing
LocalGranuleID	AST_L1B#00305312003104522_06212003111041.hdf
Calendar Date	2003-05-31
Time of Day	10:45:22 UTC
Latitude	52.44,52.28,51.73,51.88
Longitude	6.29,7.36,7.14,6.09
Measured Parameter	Registered Radiance at Sensor
Scene Cloud Coverage (%)	0
ASTER Gains	01 HGH, 02 HGH, 3N NOR, 3B NOR, 04 NOR,05 NOR, 06 NOR, 07 NOR, 08 NOR, 09 NOR
ASTER Map Projection	Universal Transverse Mercator
ASTERProcessing Center	GDS
ASTER Receiving Center	EDOS
Geometric DBVersion	02.10
Radiometric DBVersion/RCC	(The version number of the Radiometric Database used in Level 1 processing) 02.13
Resampling	NN
ASTER Map Orientation Angle	(Denotes the angle between the path oriented image and the map oriented image for this ASTER scene) 15.1218
Solar Azimuth Angle	(Angle of the sun clockwise from true North) 159.5339 (159º 32' 2.04")
Solar Elevation Angle	(Angle of the sun above the horizon) 58.5221 ($58^0$31’19”)
Collection Description	ASTER level-1B data have had system radiometric corrections and geometric coefficients applied and are re-projected to a given map projection

5.2. Appendix –B

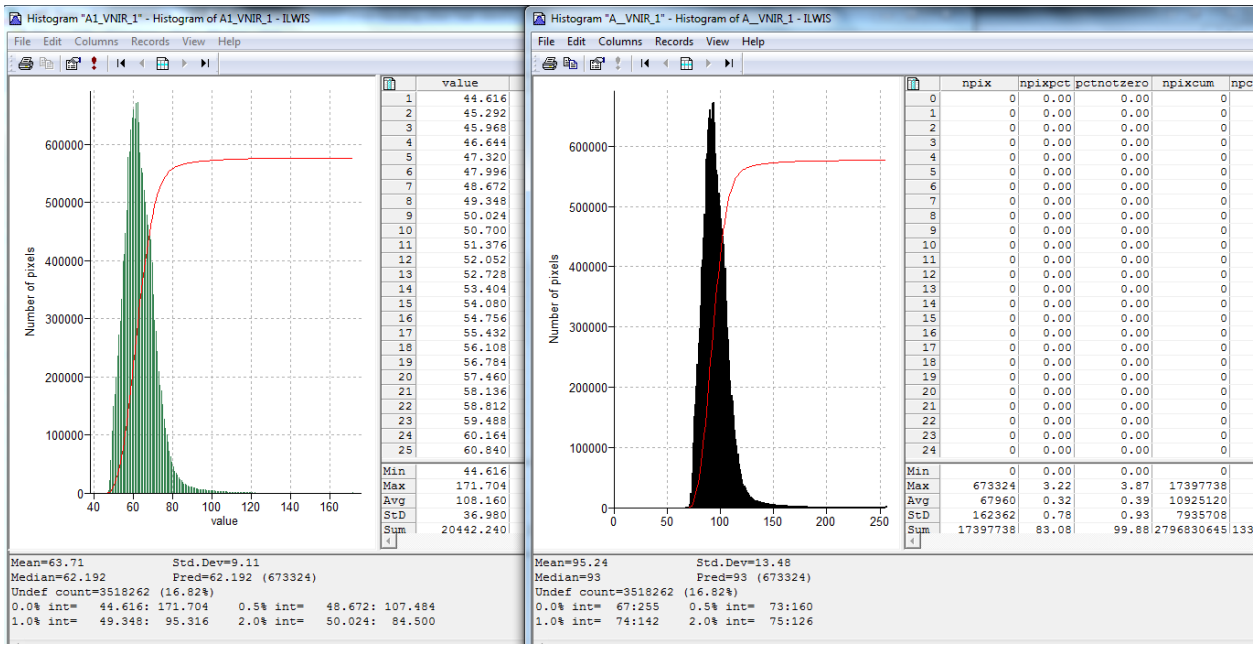

Figure 5.1 DN to radiance conversion for VNIR_1 band. Left Fig: After applying conversion formula, right Fig: Before applying conversion formula

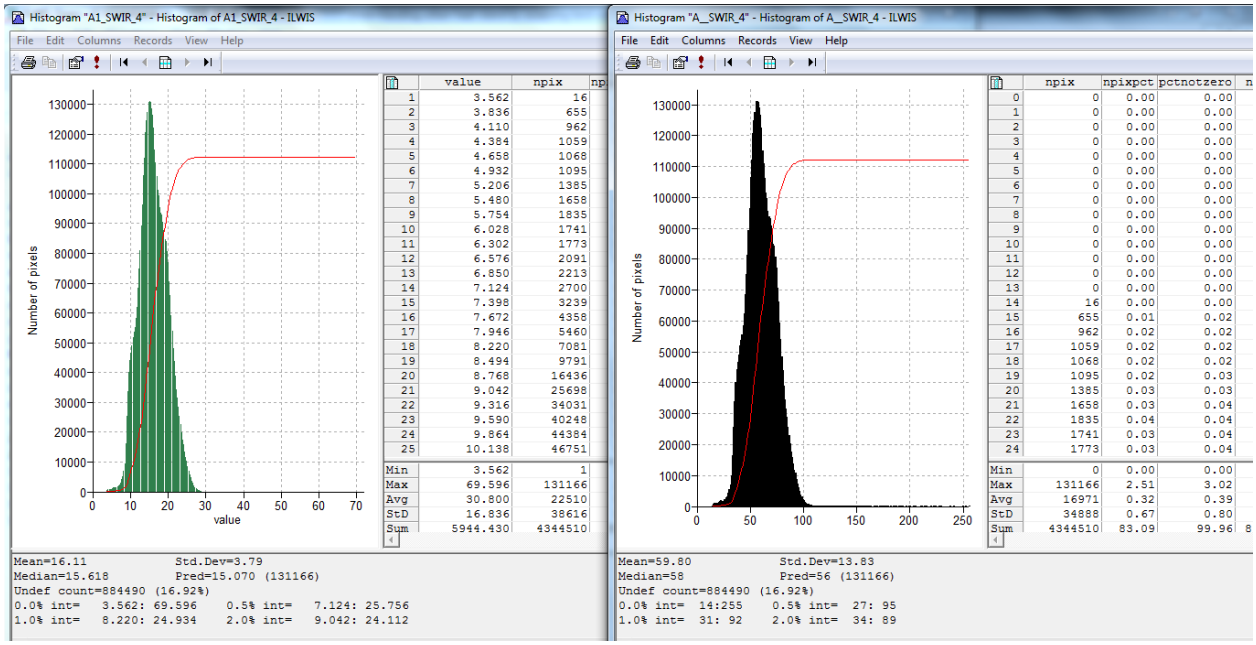

Figure 5.2 DN to radiance conversion for SWIR_4 band. Left Fig: After applying conversion formula,

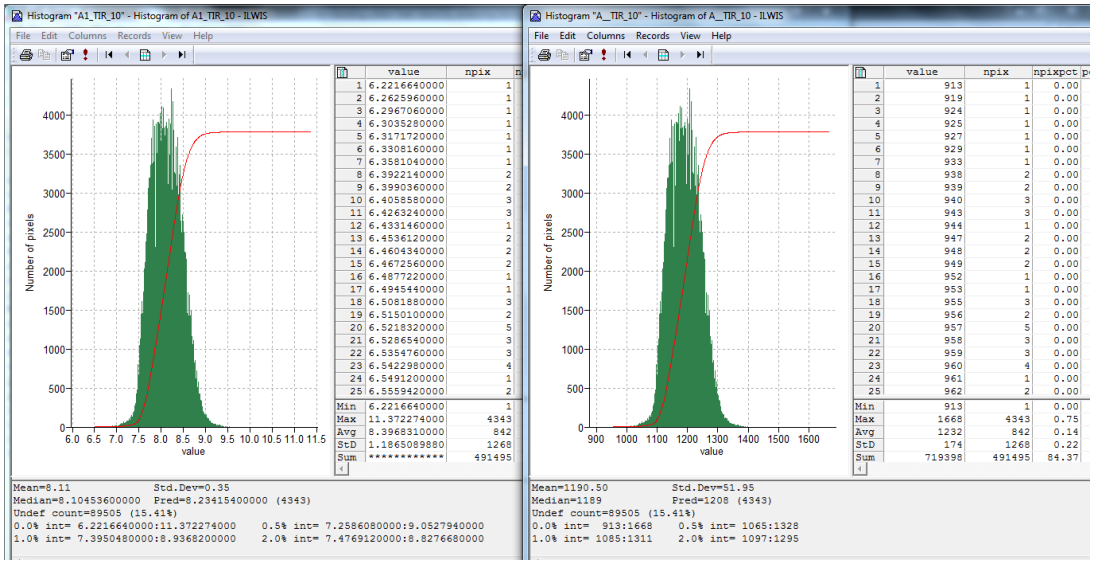

Figure 5.3 DN to radiance conversion for TIR_10 band. left Fig: after applying conversion formula, right Fig: before applying conversion formula

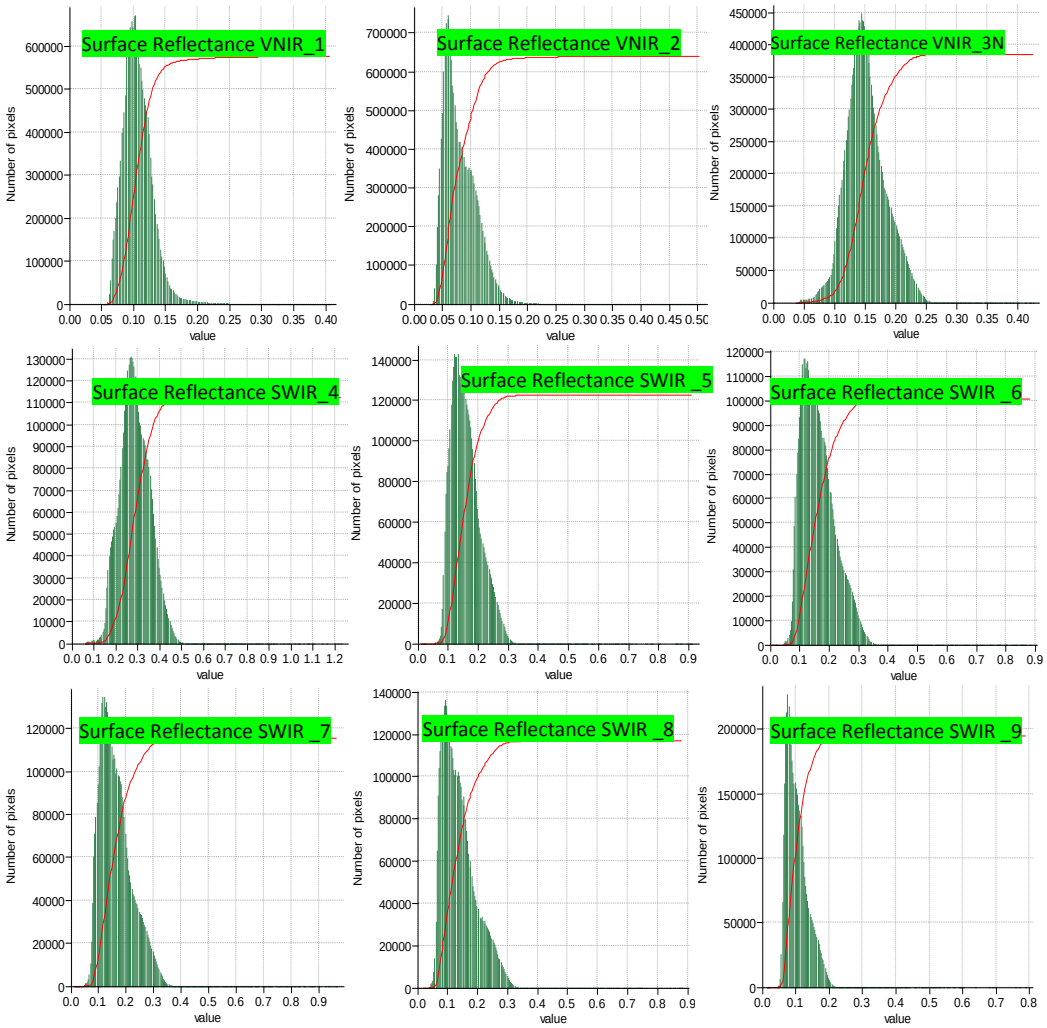

Figure 5.4 surface reflectance histogram

5.3. Appendix –C

Table 5.2 Zonal statistics of NDVI, NDBI, Albedo, Emissivity and LST respectively, where each zone represents each landuse type in Enschede

LU_TYPE/NDVI	ZONE_CODE	AREA	MIN	MAX	RANGE	MEAN	STD	MAJORITY	MINORITY	MEDIAN
Built-up	1	8450330	0.025	0.815	0.790	0.567	0.140	0.726	0.033	0.580
Rail and Road surface	2	11137300	-0.019	0.829	0.848	0.580	0.140	0.726	-0.019	0.613
Water	5	2206130	-0.069	0.834	0.903	0.596	0.143	0.726	-0.069	0.626
Forests, grassland	4	74803500	-0.234	0.834	1.068	0.599	0.138	0.726	-0.234	0.646
Cropland	3	14083400	-0.007	0.821	0.828	0.614	0.132	0.726	-0.007	0.665

LU_TYPE/NDBI	ZONE_CODE	AREA	MIN	MAX	RANGE	MEAN	STD	MAJORITY	MINORITY	MEDIAN
Built-up	1	8450330	-0.549	0.129	0.678	-0.216	0.132	-0.160	-0.549	-0.211
Water	5	2206130	-0.534	0.129	0.663	-0.225	0.149	-0.126	-0.483	-0.222
Rail and Road surface	2	11137300	-0.562	0.168	0.730	-0.221	0.141	-0.326	-0.562	-0.229
Forests, grassland	4	74803500	-0.710	0.538	1.248	-0.230	0.148	0.000	0.100	-0.256
Cropland	3	14083400	-0.554	0.142	0.696	-0.245	0.146	-0.346	-0.497	-0.281

LU_TYPE/Albedo	ZONE_CODE	AREA	MIN	MAX	RANGE	MEAN	STD	MAJORITY	MINORITY	MEDIAN
Cropland	3	14083400	0.107	0.400	0.293	0.203	0.030	0.194	0.108	0.201
Built-up	1	8450330	0.086	0.457	0.371	0.206	0.027	0.194	0.094	0.202
Rail and Road surface	2	11137300	0.093	0.469	0.376	0.207	0.029	0.191	0.093	0.204
Forests, grassland	4	74803500	0.062	0.490	0.428	0.206	0.030	0.206	0.315	0.204
Water	5	2206130	0.108	0.469	0.361	0.212	0.029	0.195	0.119	0.210

LU_TYPE/Emissivity	ZONE_CODE	AREA	MIN	MAX	RANGE	MEAN	STD	MAJORITY	MINORITY	MEDIAN
Built-up	1	8450330	0.959	0.990	0.031	0.985	0.008	0.99	0.959	0.99
Rail and Road surface	2	11137300	0.959	0.990	0.031	0.985	0.008	0.99	0.959	0.99
Cropland	3	14083400	0.959	0.990	0.031	0.986	0.007	0.99	0.959	0.99
Forests, grassland	4	74803500	0.959	0.990	0.031	0.986	0.007	0.99	0.959	0.99
Water	5	2206130	0.959	0.990	0.031	0.986	0.007	0.99	0.959	0.99

LU_TYPE/LST	ZONE_CO	AREA	MIN	MAX	RANGE	MEAN	STD	MAJORITY	MINORITY	MEDIAN
Built-up	1	8450330	285.4	312.2	26.8	299.4	3.3	295.1	287.1	299.6
Rail and Road surface	2	11137300	284.6	312.2	27.6	299.0	3.3	295.1	284.8	298.9
Water	5	2206130	284.6	309.8	25.2	298.7	3.3	296.1	287.9	298.4
Forests, grassland	4	74803500	284.6	310.5	25.9	298.5	3.3	295.1	309.6	298.2
Cropland	3	14083400	284.8	310.5	25.7	298.2	3.2	294.9	288.2	297.7

5.4. Appendix –D

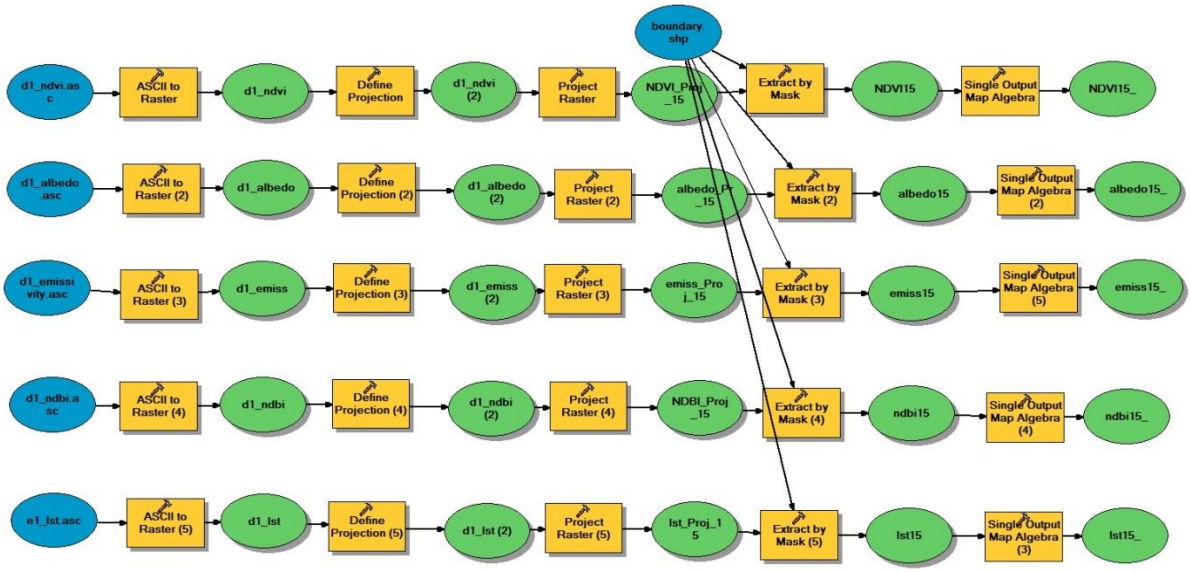

Figure 5.5 (1) Image preparation for analysis

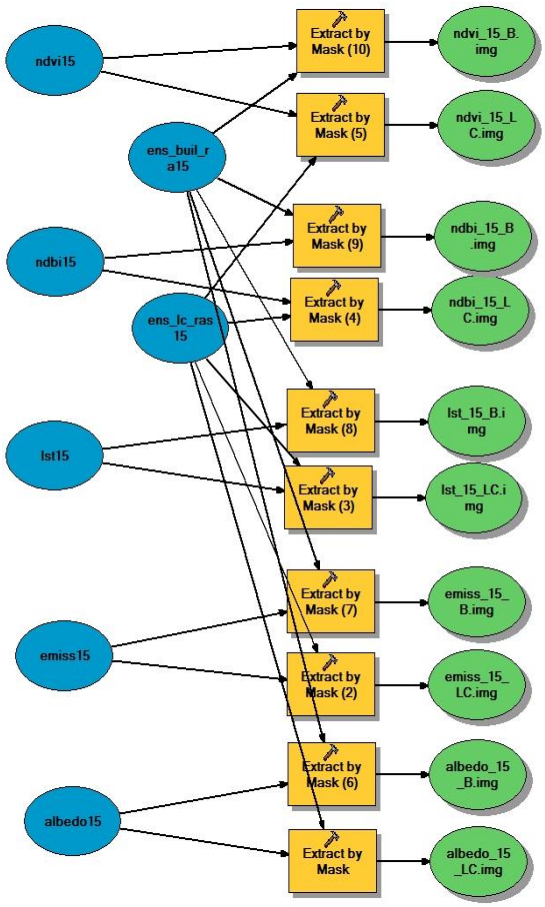

Figure 5.6 (2) Extract by mask (image and Built-up overlay)

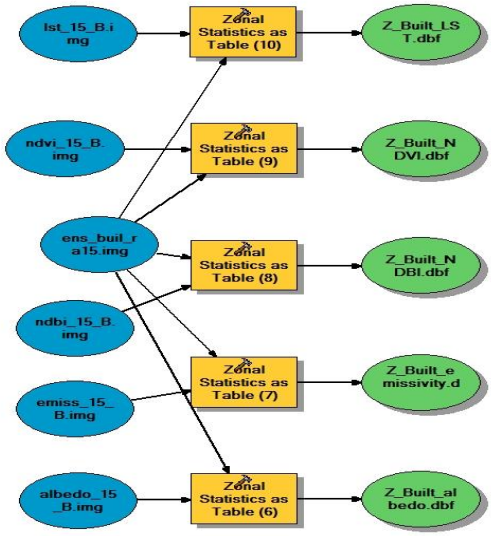

Figure 5.7 (3) Zonal statistics